



Supercooled liquid water cloud observed, analysed, and modelled at the top of the planetary boundary layer above Dome C, Antarctica

Philippe Ricaud¹, Massimo Del Guasta², Eric Bazile¹, Niramson Azouz¹, Angelo Lupi³, Pierre Durand⁴, Jean-Luc Attié⁴, Dana Veron⁵, Vincent Guidard¹, and Paolo Grigioni⁶

¹CNRM, Université de Toulouse, Météo-France, CNRS, Toulouse, France

²INO-CNR, Sesto Fiorentino, Italy

³ISAC-CNR, Bologna, Italy

⁴Laboratoire d'Aérodynamique, Université de Toulouse, CNRS, UPS, Toulouse, France

⁵University of Delaware, Newark, USA

⁶ENEA, Roma, Italy

Correspondence: Philippe Ricaud (philippe.ricaud@meteo.fr)

Received: 27 June 2019 – Discussion started: 28 August 2019

Revised: 5 March 2020 – Accepted: 6 March 2020 – Published: 7 April 2020

Abstract. A comprehensive analysis of the water budget over the Dome C (Concordia, Antarctica) station has been performed during the austral summer 2018–2019 as part of the Year of Polar Prediction (YOPP) international campaign. Thin (~ 100 m deep) supercooled liquid water (SLW) clouds have been detected and analysed using remotely sensed observations at the station (tropospheric depolarization lidar, the H₂O Antarctica Microwave Stratospheric and Tropospheric Radiometer (HAMSTRAD), net surface radiation from the Baseline Surface Radiation Network (BSRN)), radiosondes, and satellite observations (CALIOP, Cloud-Aerosol Lidar with Orthogonal Polarization/CALIPSO, Cloud Aerosol Lidar and Infrared Pathfinder Satellite Observations) combined with a specific configuration of the numerical weather prediction model: ARPEGE-SH (Action de Recherche Petite Echelle Grande Echelle – Southern Hemisphere). The analysis shows that SLW clouds were present from November to March, with the greatest frequency occurring in December and January when $\sim 50\%$ of the days in summer time exhibited SLW clouds for at least 1 h. Two case studies are used to illustrate this phenomenon. On 24 December 2018, the atmospheric planetary boundary layer (PBL) evolved following a typical diurnal variation, which is to say with a warm and dry mixing layer at local noon thicker than the cold and dry stable layer at local midnight. Our study showed that the SLW clouds were

observed at Dome C within the entrainment and the capping inversion zones at the top of the PBL. ARPEGE-SH was not able to correctly estimate the ratio between liquid and solid water inside the clouds with the liquid water path (LWP) strongly underestimated by a factor of 1000 compared to observations. The lack of simulated SLW in the model impacted the net surface radiation that was $20\text{--}30\text{ W m}^{-2}$ higher in the BSRN observations than in the ARPEGE-SH calculations, mainly attributable to the BSRN longwave downward surface radiation being 50 W m^{-2} greater than that of ARPEGE-SH. The second case study took place on 20 December 2018, when a warm and wet episode impacted the PBL with no clear diurnal cycle of the PBL top. SLW cloud appearance within the entrainment and capping inversion zones coincided with the warm and wet event. The amount of liquid water measured by HAMSTRAD was ~ 20 times greater in this perturbed PBL than in the typical PBL. Since ARPEGE-SH was not able to accurately reproduce these SLW clouds, the discrepancy between the observed and calculated net surface radiation was even greater than in the typical PBL case, reaching $+50\text{ W m}^{-2}$, mainly attributable to the downwelling longwave surface radiation from BSRN being 100 W m^{-2} greater than that of ARPEGE-SH. The model was then run with a new partition function favouring liquid water for temperatures below -20 down to -40°C . In this test mode, ARPEGE-SH has been able to generate SLW

clouds with modelled LWP and net surface radiation consistent with observations during the typical case, whereas, during the perturbed case, the modelled LWP was 10 times less than the observations and the modelled net surface radiation remained lower than the observations by $\sim 50 \text{ W m}^{-2}$. Accurately modelling the presence of SLW clouds appears crucial to correctly simulate the surface energy budget over the Antarctic Plateau.

1 Introduction

Antarctic clouds play an important role in the climate system by influencing the Earth's radiation balance, both directly at high southern latitudes and indirectly at the global level through complex teleconnections (Lubin et al., 1998). In Antarctica, there are very few observational stations and most of them are located on the coast, a fact that limits the type and characteristics of clouds observed. Nevertheless, prior studies suggest that cloud properties vary geographically, with a fractional cloud cover around the South Pole of about 50 % to 60 % in all seasons and a cloud cover of about 80 % to 90 % near the coast (Bromwich et al., 2012; Listowski et al., 2019). Based on spaceborne observations, Adhikari et al. (2012) observed that low-level cloud occurrence over the Antarctic Plateau is consistently between 20 %–50 % with the highest values occurring in winter and the lowest values consistently occurring over the Eastern Antarctic Plateau. Furthermore, cloud parameters such as the hydrometeors size and the microphysical structure are also very difficult to retrieve in Antarctica. Nevertheless, some in situ aircraft measurements exist particularly over the Western Antarctic Peninsula (Grosvenor et al., 2012; Lachlan-Cope et al., 2016) and nearby coastal areas (O'Shea et al., 2017) that provide ice mass fraction, concentration, and particle size relative to cloud temperature, cloud type, and formation mechanism, which have provided new insights into polar cloud modelling. These studies also highlighted sea ice production of cloud-condensation nuclei and ice-nucleating particles, which is important in winter both coastally and at Dome C (see, e.g., Legrand et al., 2016). Additionally, Grazioli et al. (2017) observed precipitating crystal characteristics at Dumont d'Urville using a combination of ground-based radars, in situ cameras, and precipitation sensors and looked at the role that the katabatic winds play in the formation, modification, and sublimation of ice crystals. Over the Antarctic Plateau, where the atmosphere is colder and drier than along the coast, ice crystal clouds are mainly observed with crystal sizes ranging from 5 to 30 μm (effective radius) in the core of the cloud; mixed-phase clouds are preferably observed near the coast (Listowski et al., 2019) with larger ice crystals and water droplets (Lachlan-Cope, 2010; Lachlan-Cope et al., 2016; Grosvenor et al., 2012; O'Shea et al., 2017; Grazioli et al., 2017).

The time and geographical distribution of tropospheric clouds over the Antarctic region has been recently studied using the raDAR/iDAR-MASK (DARDAR) spaceborne products (Listowski et al., 2019). The authors determined that clouds are mainly constituted of ice above the continent. The presence of supercooled liquid water (SLW, the water staying in liquid phase below 0 °C) clouds shows variations according to temperature and sea ice fraction, decreasing sharply poleward, with an abundance 2 to 3 times less over the Eastern Antarctic Plateau than over the Western Antarctic. The inability of mesoscale high-resolution models and operational numerical weather prediction models to accurately calculate the net surface radiation due to the presence of clouds (particularly of SLW clouds) in Antarctica causes biases of several tens of watts per square metres (Listowski and Lachlan-Cope, 2017; King et al., 2006, 2015; Bromwich et al., 2013) impacting the radiative budget of the Antarctic and beyond (Lawson and Gettelman, 2014; Young et al., 2019). The year-long study of mixed-phase clouds at the South Pole with a micropulse lidar presented in Lawson and Gettelman (2014) showed that SLW clouds occur more frequently than observed in earlier aircraft studies and are underestimated in models leading to biases in the surface radiation budget. In the present study, we explore these biases further, moving the focus to the modelling and simultaneous observations of low-level SLW clouds and surface radiation over the Eastern Antarctic Plateau, specifically at Dome C.

With the support of the World Meteorological Organization (WMO) World Weather Research Programme (WWRP), the Polar Prediction Project (PPP) international programme has been dedicated to the development of improved weather and environmental prediction services for the polar regions, on timescales from hours to seasons (<https://www.polarprediction.net>, last access: 2 April 2020). Within this project, the Year of Polar Prediction (YOPP), from 2018 to 2019, aims at enabling a significant improvement in environmental prediction capabilities for the polar regions and beyond, by coordinating a period of intensive observing, modelling, verification, user engagement, and educational activities. The Water Budget over Dome C (H₂O-DC) project (<https://apps3.awi.de/YPP/pdf/stream/52>, last access: 2 April 2020) has been endorsed by YOPP for studying the water budget by means of ground-based measurements of water (vapour, solid, and liquid) and clouds, by active (backscatter lidar) and passive (microwave radiometer) remote sensing, and operational meteorological analyses. The Dome C (Concordia) station is located in the Eastern Antarctic Plateau (75°06' S, 123°21' E; 3233 m above mean sea level, a.m.s.l.).

H₂O-DC concentrates on the Year of Polar Prediction Special Observing Period of measurements in the Antarctic (SOP-SH), from 16 November 2018 to 15 February 2019. During this time frame, several instruments have been employed:

1. the H₂O Antarctica Microwave Stratospheric and Tropospheric Radiometer (HAMSTRAD; Ricaud et al., 2010a) to obtain vertical profiles of temperature and water vapour, integrated water content (IWC) or precipitable water, and liquid water path (LWP), with an adjustable time resolution fixed at 60 s during the YOPP campaign.
2. the tropospheric depolarization lidar (Tomasi et al., 2015) to obtain vertical profiles of backscattering and depolarization ratio.

These two H₂O-DC data sets have been complemented in the present analysis by the three following observational data sets:

1. the Baseline Surface Radiation Network (BSRN) net surface radiances at the station.
2. the temperature profiles from radiosondes launched twice daily at the station during YOPP.
3. the spaceborne observations (backscatter and polarization) from the CALIOP (Cloud-Aerosol Lidar with Orthogonal Polarization)/CALIPSO (Cloud Aerosol Lidar and Infrared Pathfinder Satellite Observations) lidar in the vicinity of the station.

In addition, a specific Antarctic configuration of the global ARPEGE model from Météo-France (Pailleux et al., 2015) is used to characterize the water budget above Dome C considering the gas, liquid, and solid phases to study the genesis of clouds (ice or liquid).

The aim of the present study is to combine all these observations and simulations in order to (1) detect the presence of SLW clouds above Dome C, (2) analyse the formation and evolution of such SLW clouds, and (3) estimate the radiative impact of such clouds on the net surface radiation. We concentrate the analyses on two case studies observed during the YOPP campaign: one case when the planetary boundary layer (PBL) exhibited a “typical” diurnal cycle (24 December 2018) and a second case when the diurnal cycle of the PBL was perturbed by a warm and wet episode (20 December 2018).

The data sets used in our study are presented in Sect. 2. The methodology employed is explained in Sect. 3. The analyses of the SLW clouds during the typical and the perturbed PBL periods are detailed in Sects. 4 and 5, respectively. The observed and modelled impact of SLW clouds on the surface net radiation is described in Sect. 6. Section 7 includes a discussion of the results, and the conclusion synthesizes the study in Sect. 8.

2 Data sets

2.1 The HAMSTRAD

HAMSTRAD is a microwave radiometer that profiles water vapour (H₂O), liquid water, and tropospheric temperature above Dome C. Measuring at both 60 GHz (oxygen molecule line (O₂) to deduce the temperature) and 183 GHz (H₂O line), this unique, state-of-the-art radiometer was installed on site for the first time in January 2009 (Ricaud et al., 2010a, b). The measurements of the HAMSTRAD allow the retrieval of the vertical profiles of H₂O and temperature from the ground to 10 km altitude with vertical resolutions of 30 to 50 m in the PBL, 100 m in the free troposphere, and 500 m in the upper troposphere–lower stratosphere. The time resolution is adjustable and fixed at 60 s during the YOPP campaign. Note that an automated internal calibration is performed every 12 atmospheric observations and lasts about 4 min. Consequently, the atmospheric time sampling is 60 s for a sequence of 12 atmospheric measurements and a new atmospheric sequence is performed after 4 min. The temporal resolution of the instrument allows for detection and analysis of atmospheric processes such as the diurnal evolution of the PBL (Ricaud et al., 2012) and the presence of clouds and diamond dust (Ricaud et al., 2017). In addition, two other parameters can be estimated.

1. The integrated water vapour (IWV) or precipitable water (kg m^{-2}) obtained by integrating the absolute humidity profile from the surface to 10 km altitude.
2. The liquid water path (g m^{-2}), which gives the amount of liquid water integrated along the vertical.

IWV has been validated against radiosondes at Dome C between 2010 and 2014 showing a 5%–10% wet bias of HAMSTRAD compared to the sondes (Ricaud et al., 2015) that were uncorrected for sensor heating or time lag effect, which may produce a 4% dry bias (Miloshevich et al., 2006). The 1σ rms error in the 7 min integration time IWV is 0.05 kg m^{-2} or $\sim 5\%$ (Ricaud et al., 2013).

The HAMSTRAD-observed LWP was only presented when the instrument was installed at the Pic du Midi station (2877 a.m.s.l., France) during the calibration or validation period in 2008 prior to its set-up in Antarctica in 2009 (Ricaud et al., 2010a). Because the instrument has been designed and developed for measuring water vapour in very dry and cold environments such as those encountered at the Dome C station all year long, the radiometer functionality is better adapted for the Dome C site than for the Pic du Midi site. It has not been possible to validate LWP observations at the Pic du Midi station. The H₂O-DC project has thus provided a unique opportunity to perform such a qualitative validation against lidar observations of SLW.

2.2 The tropospheric depolarization lidar

A tropospheric depolarization lidar (532 nm) has been operating at Dome C since 2008 (see http://lidarmax.altervista.org/englidar/_AntarcticLIDAR.php, last access: 2 April 2020). The lidar provides 5 min tropospheric profiles of aerosols and clouds continuously, from 20 to 7000 m above ground level (a.g.l.), with a resolution of 7.5 m. Lidar depolarization (Mishchenko et al., 2000) is a robust indicator of non-spherical shape for randomly oriented cloud particles. A depolarization ratio below 10 % is characteristic of SLW clouds, while higher values are produced by ice particles. The possible ambiguity between SLW clouds and oriented ice plates is avoided at Dome C by operating the lidar 4° off-zenith (Hogan and Illingworth, 2003). The lidar observations at Dome C have already been used to study the radiative properties of water vapour and clouds in the far infrared (Palchetti et al., 2015). As a support to lidar data interpretation, time-lapse webcam videos of local sky conditions are also collected.

2.3 The BSRN

The BSRN sensors at Dome C are mounted at the Astrocordia and Albedo Rack sites, with upward- and downward-looking, heated, and ventilated standard Kipp&Zonen CM22 pyranometers and CG4 pyrgeometers providing measurements of hemispheric downward and upward broadband shortwave (SW, 0.3–3 μm) and longwave (LW, 4–50 μm) fluxes at the surface, respectively. These data are used to retrieve values of net surface radiation (defined as the difference between the downward and upward fluxes). All these measurements follow the rules of acquisition, quality check, and quality control of the BSRN (Driemel et al., 2018).

2.4 Radiosondes

Vertical temperature and humidity profiles have been measured on a daily basis at Dome C since 2005, employing RS92 Vaisala radiosondes. The radiosonde data were taken using the standard Vaisala evaluation routines without any correction of sensor heating or time lag effect. The sondes are known to have a cold bias of 1.2 K from the ground to about 4 km altitude (Tomasi et al., 2011 and 2012) and a dry bias of 4 % on IWV (Miloshevish et al., 2006), mainly between 630 and 470 hPa, with a correction factor for humidity varying within 1.10–1.15 for daytime (Miloshevish et al., 2009). During YOPP and the two case studies, launches were performed twice per day at 00:00 and 12:00 Universal Time Coordinated (UTC).

2.5 CALIOP on board CALIPSO

Orbiting at 705 km altitude, the CALIPSO mini-satellite has been observing clouds and aerosols since 2006 to better understand the role of clouds and aerosols in climate. To ac-

complish this mission, the CALIPSO satellite is equipped with a lidar, a camera, and an infrared imager (Winker et al., 2009). CALIOP is a dual-wavelength (532 and 1064 nm) backscatter lidar. It provides high-resolution vertical profiles of clouds and aerosols along the orbit track (Young and Vaughan, 2009). We have used version V3.40 data retrieved from <https://www-calipso.larc.nasa.gov/> (last access: 2 April 2020).

2.6 The ARPEGE-SH model

A special Antarctic configuration of the operational global model ARPEGE was used for the YOPP SOP-SH period (16 November 2018–15 February 2019). This configuration named ARPEGE-SH is based on the operational global model used for numerical weather prediction (NWP) ARPEGE (Pailleux et al., 2015), but with its highest horizontal resolution centred over Dome C instead of over France, as set-up in ARPEGE. A 4D variational (4DVar) assimilation was performed every 6 h. The meteorological analyses were given by the ARPEGE-SH system together with the 24 h forecasts at the node the closest to the location of Dome C. Two analyses at 00:00 and 12:00 UTC were represented in the present study together with hourly forecasts initialized by the two analyses from 01:00 to 11:00 and from 13:00 to 24:00 UTC. The horizontal resolution during the SOP-SH period was 7.5 km at Dome C. The vertical resolution during the SOP-SH period was constituted by 105 vertical levels, the first one being set at 10 m, with 12 levels below 1 km and 35 levels below 3 km. Several ARPEGE-SH output parameters were selected for analysis: cloud fraction, ice, water vapour and liquid water mixing ratio, temperature, total column ice (TCI, ice integrated along the vertical), LWP, IWV, and net surface radiation. For each of the model vertical levels, the value of the cloud fraction ranges between 0 and 1 and is defined as the fraction of the cloud within the model horizontal grid box. The total cloud fraction at each level is a combination between the resolved cloud, the cloud from the shallow convection and the cloud from the deep convection. The resolved cloud is based on a pdf function with a critical relative humidity profile. The shallow convection cloud (below 4000 m) is based on the cloud water or ice tendencies computed by the shallow mass flux scheme with a maximum value at 0.3. For the deep convection, the cloudiness is computed with the vertical divergence of the precipitation flux. The diurnal variation in the top of the PBL is calculated by ARPEGE-SH as the level where the turbulence kinetic energy becomes lower than $0.01 \text{ m}^2 \text{ s}^{-2}$.

2.7 The NCEP temperature fields

In order to assess the synoptic state of the atmosphere during the two case studies above Dome C against the climatological state of the atmosphere in summer over Antarctica, we have used the temperature fields at 600 hPa from the National

Centers for Environmental Prediction (NCEP) from 2009 to 2019 (Kanamitsu et al., 2002). These are NCEP Department of Energy (NCEP/DOE) Atmospheric Model Intercomparison Project (AMIP-II) Reanalysis (Reanalysis-2) 6-hourly air temperature at $2.5^\circ \times 2.5^\circ$ horizontal resolution over the globe.

2.8 The HYSPLIT back trajectories

In order to assess the origin of air masses associated with the two case studies, 10 d back trajectories originating from the Dome C station at 500 and 1000 m above ground level have been calculated on 20 and 24 December 2018 at 12:00 UTC from the Hybrid Single-Particle Lagrangian Integrated Trajectory model (HYSPLIT) model (Stein et al., 2015; Rolph et al., 2017) (<https://www.ready.noaa.gov/HYSPLIT.php>, last access: 2 April 2020).

3 Methodology

In this article, we present two case studies from the SOP-SH that illustrate the occurrence of low-level SLW clouds at Dome C. Both cases occurred in December 2018, within 5 d of each other, which allows direct comparison between the cases without concerns for seasonal variations in radiation.

The first case study presented was on 24 December 2018 and was representative of a climatological summer atmosphere in contrast to the second case study (20 December 2018) when the atmosphere was very different from a climatological summer atmosphere. We have considered in Fig. 1 the temperature fields from the NCEP at 600 hPa to highlight the state of the atmosphere above Antarctica with a focus over the Dome C station at different periods: (a) decadal average over December–January from 2009 to 2019, (b) YOPP average over December 2018–January 2019, (c) daily average over 24 December 2018, (d) 20 December 2018 at 00:00 UTC, (e) 20 December 2018 at 12:00 UTC, and (f) 21 December 2018 at 00:00 UTC. The climatological summer temperature field at 600 hPa has been calculated by averaging the December and January data from 2009 to 2019, and the mean synoptic state of the YOPP campaign during the summer 2018–2019 has been calculated by averaging data from early December 2018 to end of January 2019. The synoptic state of the first case study was selected on 24 December 2018 averaged from 00:00 to 24:00 UTC and for the second case study on 20 December 2018 at 00:00 UTC and 12:00 UTC and on 21 December 2018 at 00:00 UTC. Firstly, the summer atmosphere during YOPP was very consistent with the decadal climatological state of the atmosphere both over Antarctica and the Dome C station (temperature less than 245 K). Secondly, the synoptic state of the atmosphere on 24 December 2018 (first case study), although warmer (> 258 K) over some parts of the Antarctic Plateau (60 – 90° E), is, over Dome C, consistent with the YOPP summer

synoptic state and the climatological summer temperatures of ~ 246 K. Thirdly, on 20 December 2018 (second case study), a tongue of warm air (254 – 260 K) originating from the oceanic coast in the sector 0 – 30° W (00:00 UTC) reaches Dome C 24 h later with temperatures increasing from 252 to 256 K, about 10 K greater than on 24 December 2018. Ten-day back trajectories calculated from HYSPLIT (see Fig. S1 in the Supplement) initiated at Dome C at 500 and 1000 m a.g.l. remain over the Antarctic Plateau on 24 December 2018 (first case study), whereas they originated at the oceanic coast in the sector 0 – 30° W on 20 December 2018 (second case study). This is consistent with previous studies (Ricaud et al., 2017) showing that inland-originating air masses bring cold and dry air to Dome C, whilst ocean-originating air masses bring warm and wet air to Dome C.

In the following, we will label the first case study on 24 December 2018 the typical case and the second case study the perturbed case. We will show that, in the typical case, the SLW cloud occurred over a 24 h period that was characterized by a typical summertime, diurnal PBL cycle, where the mixed-layer develops over the course of the day, reaches quite a stable height, and then collapses to the surface toward the end of the day, around 12:00 UTC (Ricaud et al., 2012). The first case provides insight into the impact of SLW clouds on the local radiative fluxes. The perturbed case provides a contrasting situation where the diurnal cycle of the PBL was perturbed by the sudden arrival of very moist and warm air of oceanic origin (see Ricaud et al., 2017). We analyse how this episode affected the presence and evolution of SLW clouds and their influence on the surface energy budget. Note that, in the remainder of the article, the data will be presented according to their height above ground level (a.g.l.) unless explicitly shown as above mean sea level (a.m.s.l.).

4 Typical diurnal cycle of the PBL

The first case study occurred on 24 December 2018 during a typical diurnal PBL cycle. All the results are presented in UTC with local time (LT) being 8 h ahead of UTC ($LT = UTC + 8$ h). As described in Ricaud et al. (2012), the typical summer boundary layer at Dome C is very similar to that described by Stull (2012). Although sunlight is present throughout the day, the variation in magnitude is enough to allow a stable boundary layer from 18:00 to 06:00 LT, similar to a stable nocturnal boundary layer. There is then a transition from a stable boundary layer to a mixed layer around 06:00 LT with the increase in the solar irradiation, which reaches a maximum around solar noon. Then around 18:00 LT, the stable boundary layer starts to form again, with a quasi-mixed layer about it. The height of the summertime boundary layer at Dome C typically ranges between 100 and 400 m. The presence of SLW clouds at the top of the PBL together with the diurnal evolution of the PBL will be discussed in more detail in Sect. 7.2.

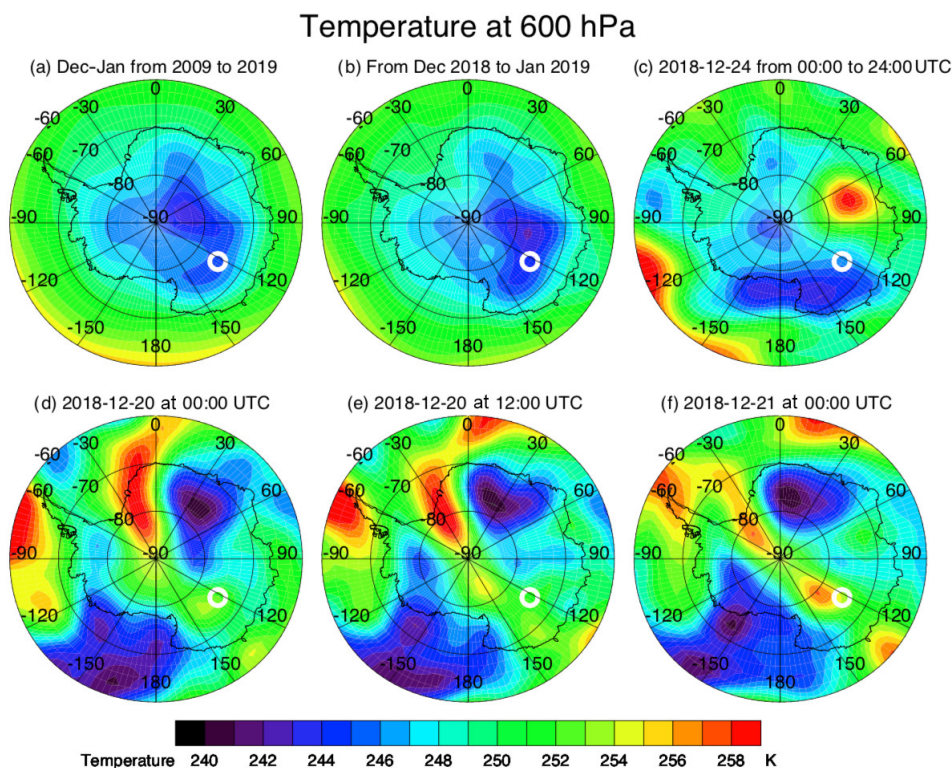


Figure 1. Temperature fields from NCEP at 600 hPa: (a) decadal average over December–January from 2009 to 2019, (b) YOPP average over December 2018–January 2019, (c) daily average over 24 December 2018, (d) 20 December 2018 at 00:00 UTC, (e) 20 December 2018 at 12:00 UTC, and (f) 21 December 2018 at 00:00 UTC. The white circle represents the position of the Dome C station.

4.1 Clouds

The presence of clouds is highlighted by the lidar backscatter and depolarization profiles shown in Fig. 2a and b, respectively. High values of lidar backscatter ($\beta > 100\beta_{\text{mol}}$, with β_{mol} the molecular backscatter) indicate that clouds and/or precipitation are present intermittently throughout the day with some significant differences. First, vertical “stripes” of high backscatter values are visible from 10 to 400 m height before 10:00 UTC and after 19:00 UTC, associated with high values of depolarization ratio ($> 20\%$), characteristic of precipitating ice crystals. Second, high values of β associated with a very low depolarization ratio ($< 5\%$) occur within a thin layer of approximately 100 m depth around 500 m from 08:00 to 22:00 UTC, with some breaks around 11:00 and 19:00–21:00 UTC. From the lidar observations, this combination of high backscatter and low depolarization ratio signifies the presence of an SLW cloud (Fig. 2c).

The NWP model ARPEGE-SH calculates cloud fraction, ice water, and liquid water mixing ratios (kg kg^{-1}) for 24 December 2018 (Fig. 3a, b, and c, respectively). We note that the outputs from ARPEGE-SH at 00:00 and 12:00 UTC are the analyses and, for the remaining time, the outputs are the hourly forecasts. ARPEGE-SH predicts the presence of clouds (cloud fraction > 0.95) for most of the day except

around 11:00 and 23:00 UTC (Fig. 3a). Before 12:00 UTC, the cloud is mainly confined to between 300 and 600–800 m, whilst, after 12:00 UTC, it spreads from the surface to 800 m. There are also high-level clouds at 2000–3000 m height but with a cloud fraction between 0.50 and 0.70. The majority of the clouds produced by ARPEGE-SH are mainly composed of ice crystals (Fig. 3b) with some traces of droplets (Fig. 3c) due to the model’s partitioning between ice and liquid where all condensed water is ice below -20°C . The liquid water clouds derived from the lidar observations are superposed over the SLW clouds calculated by ARPEGE-SH. The modelled values of liquid water ($\sim 4 \times 10^{-6} \text{ g m}^{-3}$) are very low, far lower than the values of 0.1 g m^{-3} observed for coastal polar stratus clouds (see, e.g., O’Shea et al., 2017; Lachlan-Cope et al., 2016; Young et al., 2016). It is evident that ARPEGE-SH fails in estimating (1) the vertical distribution of liquid water (a thin layer is observed around 500 m, whereas the modelled cloud layer extends from the surface to 800 m); (2) its temporal evolution (presence of SLW cloud almost all day long in ARPEGE-SH compared to SLW clouds from 08:00 to 22:00 UTC in the observations); and (3) the liquid vs. ice mixing ratio, the former being several orders of magnitudes lower in the model than the latter, in contrast to the observations.

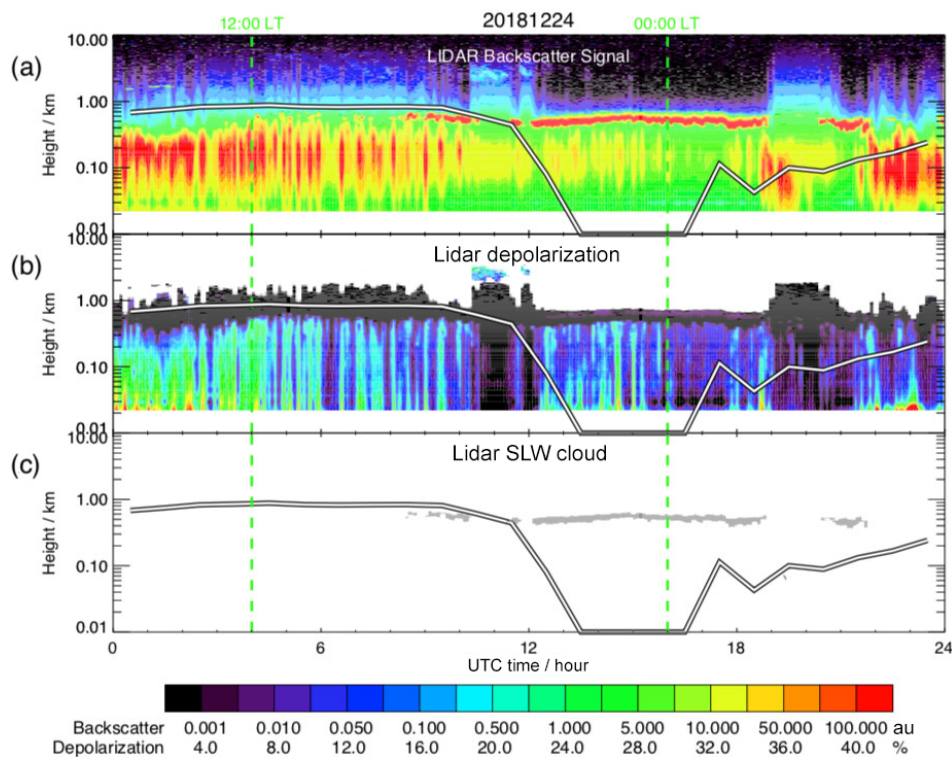


Figure 2. Diurnal variation on 24 December 2018 (UTC time) along the vertical of (a) the backscatter signal (arbitrary unit, A.U.), (b) the depolarization ratio (%) measured by the aerosol lidar, and (c) the supercooled liquid water (SLW) cloud height (grey) deduced from the aerosol lidar ($\beta_c > 100\beta_{\text{mol}}$, depolarization $< 5\%$). Superimposed on all the figures is the top of the planetary boundary layer calculated by the ARPEGE-SH model (black–white thick line). Two vertical green dashed lines indicate 12:00 and 00:00 LT.

The diurnal variation along the vertical of the total snow flux (mm d^{-1}) calculated by ARPEGE-SH on 24 December and on 20 December 2018 is shown in Figs. S2 and S3, respectively. On 24 December 2018 (Fig. S2), ARPEGE-SH forecasts some solid precipitation between 00:00 and 10:00 UTC from ~ 500 m a.g.l. to the surface consistently with the lidar observations (Fig. 2a and b). On 20 December 2018 (Fig. S3), ARPEGE-SH calculates trace amounts of solid precipitation close to the surface around 16:00 UTC consistently with the lidar observations (Fig. 9a and b). ARPEGE-SH was thus able to forecast solid precipitation during the two case studies.

The presence of clouds above the station can also be inferred from vertically integrated variables such as (1) TCI calculated by ARPEGE-SH, (2) LWP from HAMSTRAD and ARPEGE-SH, and (3) IWV from HAMSTRAD and ARPEGE-SH (Fig. 4a, b, and c, respectively). The ARPEGE-SH TCI on 24 December 2018 (Fig. 4a) oscillates between 10 and 30 g m^{-2} except around 12:00 UTC when a clear minimum occurs ($\sim 3 \text{ g m}^{-2}$), underscoring the fact that ARPEGE-SH obtains ice clouds for the entire day, except at 12:00 UTC. The HAMSTRAD LWP shows an obvious increase from ~ 1.0 to ~ 2.0 – 3.0 g m^{-2} when the presence of SLW cloud is indicated by lidar observations (Fig. 4b).

The ARPEGE-SH LWP is, on average, 10^3 times lower than that observed by HAMSTRAD, highlighting the fact that ARPEGE-SH misrepresents features of the SLW clouds over Dome C. The 1σ rms error in the 1 min integration time for the HAMSTRAD LWP can be estimated to be $\sim 15\%$. Based on the comparisons between the HAMSTRAD LWP and the lidar observations of SLW clouds during the YOPP campaign, we can estimate that the LWP bias is about 1.0 g m^{-2} . We cannot rule out that these biases might also be related in part to differences in the observation wavelengths employed (submicron particles for the lidar and microwaves for HAMSTRAD) that could favour large particles (HAMSTRAD) over small particles (lidar). Biases might also be due to the observing geometry that differs between the lidar (close to zenith viewing) and HAMSTRAD (atmospheric scans at 10 angles from zenith to $\sim 3^\circ$ elevation). HAMSTRAD and ARPEGE-SH IWV (Fig. 4c) vary from 0.65 to 1.05 kg m^{-2} throughout the day on 24 December 2018, with an agreement to within 0.1 kg m^{-2} (i.e. $\sim 10\%$ – 15%), which is consistent with previous studies (Ricaud et al., 2017).

Observation of clouds from spaceborne sensors has two main advantages: (1) it complements the ground-based cloud observations at Dome C (namely ice or liquid water), and (2) it provides an estimate of the vertical and horizontal ex-

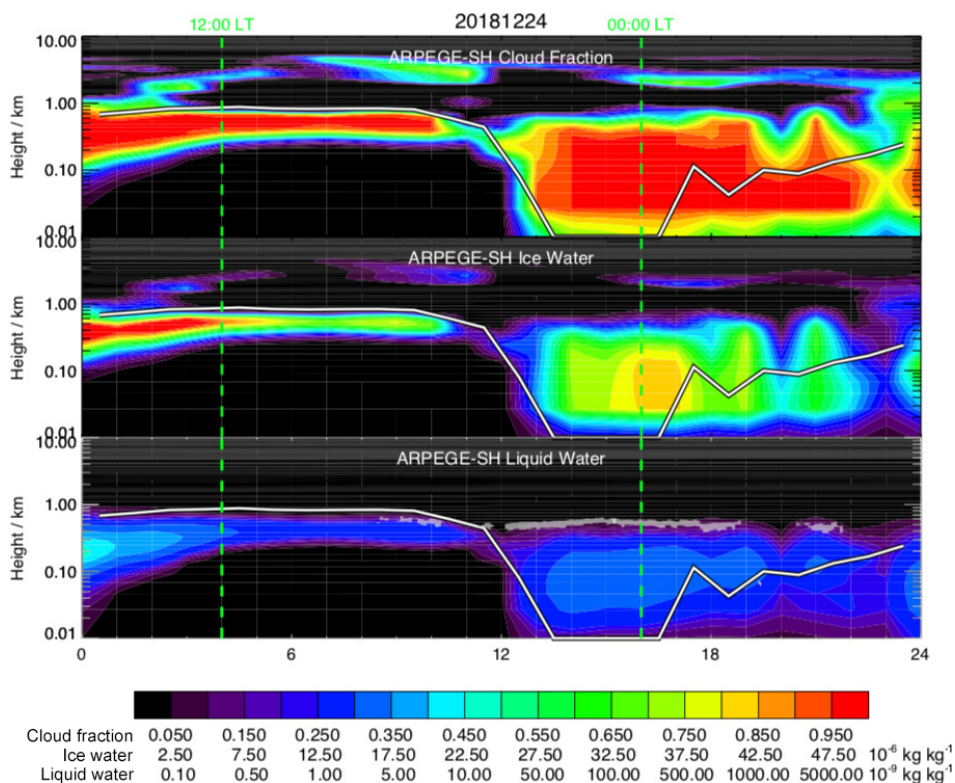


Figure 3. Time–height cross section on 24 December 2018 (UTC time) of (a) the cloud fraction (0–1), (b) the ice water mixing ratio (10^{-6} kg kg $^{-1}$), and (c) the liquid water mixing ratio (10^{-9} kg kg $^{-1}$) calculated by the ARPEGE-SH model. Superimposed on all the panels is the top of the planetary boundary layer calculated by the ARPEGE-SH model (black–white thick line). Superimposed on panel (c) is the SLW cloud (grey area) deduced from the lidar observations (see Fig. 1c). Two vertical green dashed lines indicate 12:00 and 00:00 LT.

tents of the detected cloudy layers. Note that the CALIPSO spaceborne lidar operates at the same wavelength as the backscatter lidar at Dome C, with the same method for discriminating ice from liquid water. Consequently, the two lidars should give consistent information for the detected cloud phase. However, the presence of an optically thick cloud may extinguish the CALIOP signal underneath as was already presented in Ricaud et al. (2017) when studying episodes of thick (5 km deep) clouds and diamond dust (ice crystals in suspension close to the surface). The main difficulty with this approach is related to the temporal and spatial sampling of the spaceborne instrument, namely finding a satellite overpass coincident both in time and location with the cloud observed at Dome C. This, unfortunately, decreases the number of overpasses that are scientifically exploitable. Nevertheless, on 24 December 2018, two orbits of CALIOP/CALIPSO passed close to Dome C at times when SLW clouds were observed by ground-based instruments. We show the vertical feature mask and ice or water phase from the pass closest to the station (~ 220 km), from 15:50 to 16:03 UTC (Fig. 5a and b, respectively). Firstly, we note the presence of a cloud a few hundred metres deep near the surface in the vicinity of Dome C (Fig. 5a; note that the CALIOP/CALIPSO altitude is above sea level and Dome C

is at an altitude of 3233 m a.m.s.l.). Secondly, this cloud is composed of SLW (Fig. 5b), confirming the analysis based on the observations from the lidar and the HAMSTRAD. Furthermore, we can state that this SLW cloud is not a local phenomenon but has a horizontal extent of ~ 450 km along the orbit track. Considering the CALIOP total and perpendicular attenuated backscatter data at 532 nm on 24 December 2018 at 16:00 and 14:00 UTC (Figs. S4 and S5, respectively), we note that (1) the SLW cloud is located between 3.7 and 3.8 km a.m.s.l., that is to say a height from ~ 450 to ~ 550 m a.g.l., and (2) since the CALIOP signal is able to reach the surface underneath the SLW cloud, ice is not detected by the spaceborne instrument. This is consistent with the observations performed at Dome C. The other orbit from 14:11 to 14:25 UTC (Fig. S6) is slightly more distant than the one shown in Fig. 5 (~ 360 km), but it exhibits a similar SLW cloud located between ~ 450 and ~ 550 m a.g.l., over an even greater horizontal extent of ~ 700 km along the orbit track.

4.2 Vertical profiles of temperature and water vapour

On 24 December 2018, temperatures from both HAMSTRAD and ARPEGE-SH ranged from 240 to 250 K (-33 to

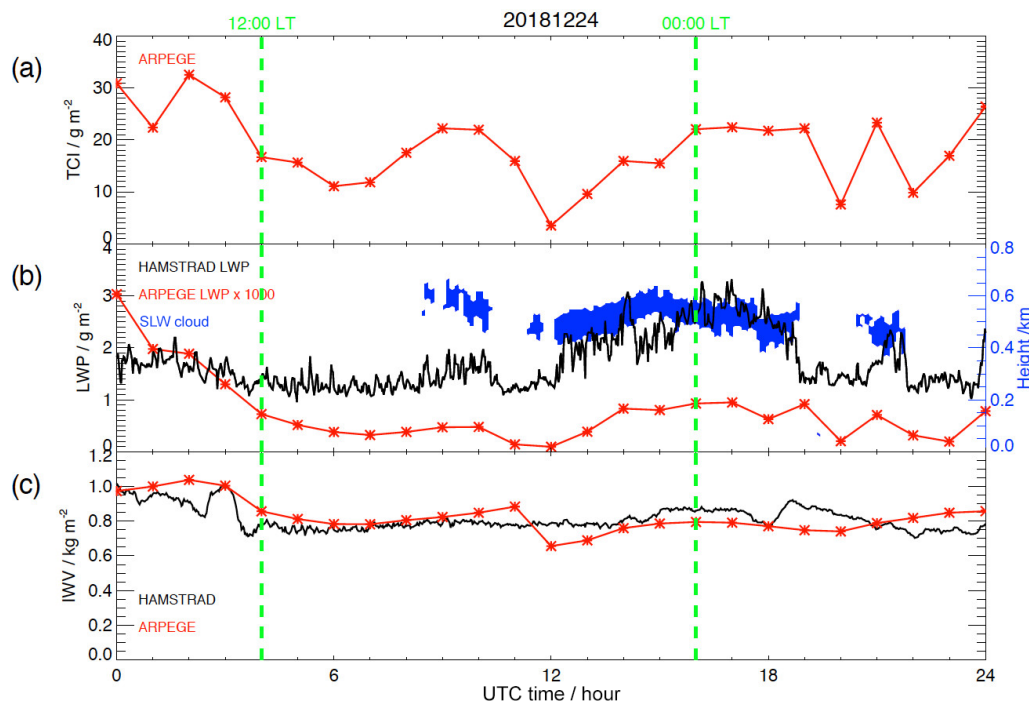


Figure 4. Diurnal variation on 24 December 2018 (UTC time) of (a) the total column of ice (TCI) (g m^{-2}) calculated by ARPEGE-SH (red crossed line), (b) the liquid water path (LWP) measured by HAMSTRAD (g m^{-2} , black solid line) and calculated by ARPEGE-SH ($\times 1000 \text{ g m}^{-2}$, red crossed line), and (c) the integrated water vapour (IWV, kg m^{-2}) measured by HAMSTRAD (black solid line) and calculated by ARPEGE-SH (red crossed line). Superimposed on panel (b) is the SLW cloud thickness (blue area) deduced from the lidar observations (see Fig. 1c) (blue y axis on the right of the figure). Note LWP from ARPEGE-SH has been multiplied by a factor of 1000. Two vertical green dashed lines indicate 12:00 and 00:00 LT.

-23°C) from the surface to 1 km a.g.l., compatible with the presence of SLW clouds. The diurnal variations in temperature and water vapour anomalies calculated by ARPEGE-SH and measured by HAMSTRAD are shown in Fig. 6. For each height, the daily averaged value has been subtracted. This has the advantage of highlighting areas of maximum and minimum changes along the vertical, and it reduces biases when comparing the two data sets. Absolute anomalies (K) are presented for temperatures, whilst relative anomalies (%) are shown for water vapour.

The diurnal variation in the ARPEGE-SH temperature (Fig. 6a) from the surface to 1 km shows a warm atmosphere before 12:00 UTC and a fast cooling one afterward. HAMSTRAD shows a similar cooling (Fig. 6b), but the transition is not so abrupt and occurs later, around 15:00 UTC. The diurnal amplitude is greater in ARPEGE-SH ($\sim 5 \text{ K}$) than in HAMSTRAD ($\sim 3 \text{ K}$). The diurnal variation in the water vapour in ARPEGE-SH (Fig. 6c) from the surface to 1 km shows a wet atmosphere before 12:00 UTC and a drier atmosphere afterwards, again with an abrupt transition. From HAMSTRAD, the diurnal variation in the water vapour (Fig. 6d) from the surface to 1 km is more complex, alternating wet and dry phases, which is particularly obvious at 500 m alti-

tude: wet (00:00–03:00 UTC), dry (03:00–08:00 UTC), wet (08:00–09:00 UTC), dry (09:00–12:00 UTC), wet (12:00–22:00 UTC), and dry (22:00–24:00 UTC). The time evolution of the SLW cloud (Fig. 2c) and the diurnal variation in the top of the PBL as calculated by ARPEGE-SH are superposed on all the panels of Fig. 6. We note that the SLW cloud appeared just below the ARPEGE-SH-estimated PBL top, around 08:00 UTC, and persisted around the same altitude after 12:00 UTC even though the PBL top had dramatically decreased down to the surface. In addition, the SLW cloud persisted after 12:00 UTC in a layer that is cooler than earlier in the day but slightly warmer than the air above and below it. However, the model shows that this layer is drier, while the observations suggest it is wetter.

4.3 Potential temperature gradient

We now consider the mechanisms that allow the SLW cloud to persist in a thin layer (about 100 m deep) around 500–600 m altitude. Even if the PBL gets thinner after 12:00 UTC, a residual mixed layer remains above (see, e.g., Fig. 1.7 of Stull, 2012; Fig. 12 top of Ricaud et al., 2012, and definition of a residual layer from the American Meteorological Society at http://glossary.ametsoc.org/wiki/Residual_layer, last access: 2 April 2020). This layer, where turbulence is spo-

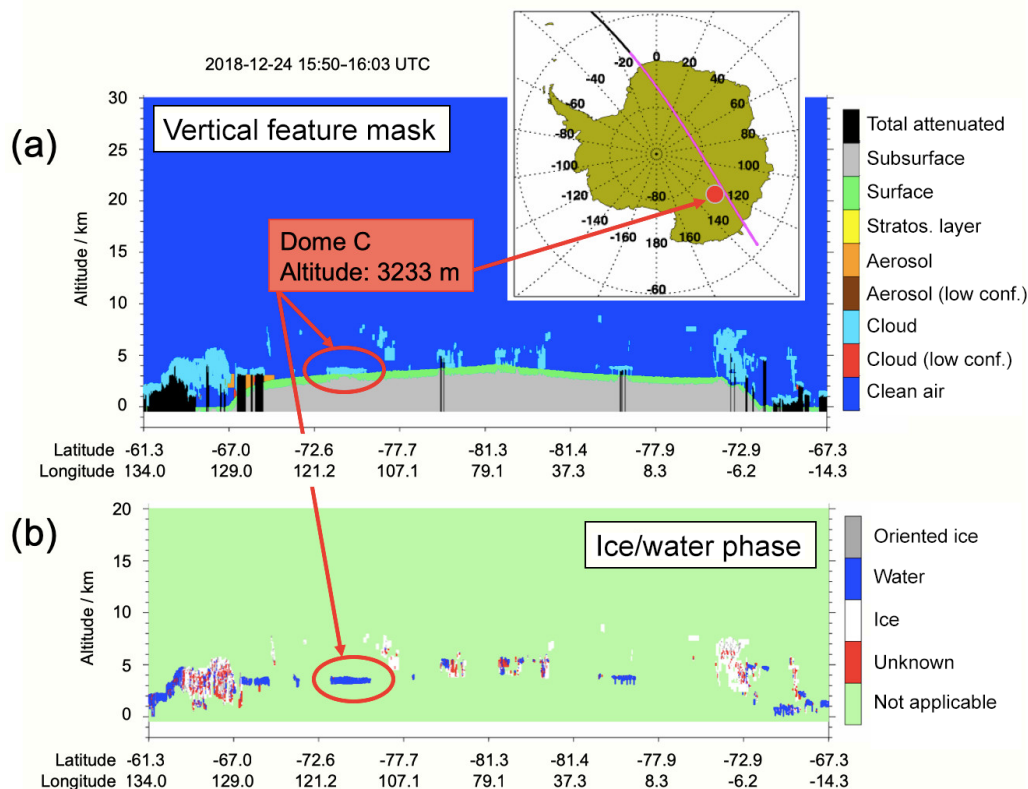


Figure 5. CALIOP/CALIPSO spaceborne lidar observations version V3.40 along one orbit on 24 December 2018 (15:50–16:03 UTC) in the vicinity of Dome C (75° S, 123° E): (a) the vertical feature mask highlighting a cloud (light blue) near the surface (red circle) and (b) the ice or water phase mask highlighting an SLW (dark blue) cloud near the surface (red circle). The ground track of the sensor (pink) has been embedded at the top of the figure, with the location of Dome C marked (red filled circle). Note that the altitude is relative to the sea surface, with the height of surface of Dome C at an elevation of 3233 m a.m.s.l. Figure adapted from the original image available at https://www-calipso.larc.nasa.gov/products/lidar/browse_images/std_v34x_showdate.php?browse_date=2018-12-24 (last access: 3 April 2020).

radic or even absent, lies above the surface-connected stable layer and can be viewed as a fossil of the mixed layer developed during the previous mixing period. The transition from the boundary layer to the free atmosphere is characterized by a local maximum of the potential temperature (θ) vertical gradient ($\partial\theta/\partial z$).

Figure 7 shows the $\partial\theta/\partial z$ field and the evolution of the mixed layer top, both computed from ARPEGE-SH output – the latter defined according to whether the turbulent kinetic energy exceeds a defined threshold – and the observed SLW cloud superposed. Black areas correspond to neutral conditions ($\partial\theta/\partial z \sim 0$), whereas the coloured ones relate to stable stratification according to the colour scale in the figure. The SLW cloud, once it has appeared at the top of the PBL around 08:00 UTC, persists after 12:00 UTC in a layer around 500–600 m coinciding with the top of the residual mixed layer (see above for the definition) even after the ARPEGE-defined mixed layer top collapses down to the surface.

Figure 8a, b, and c show the vertical profiles of θ (K) and $\partial\theta/\partial z$ (K km^{-1}) as calculated from temperature measured by the radiosondes and analysed by ARPEGE-SH at

Dome C on 24 December 2018 at 00:00 and 12:00 UTC and on 25 December 2018 at 00:00 UTC. The presence and the depth of the SLW cloud detected from lidar observations are highlighted in the figure. The atmosphere as analysed by ARPEGE-SH is about 3–5 K warmer than the observations. From 100 m upward, the maximum of $\partial\theta/\partial z$ is measured at 400, 550, and 600 m on 24 December 2018 at 00:00 and 12:00 UTC and on 25 December 2018 at 00:00 UTC, respectively, with an amplitude of 10, 12, and 40 K km^{-1} , respectively. ARPEGE-SH cannot reproduce the fine vertical structure of $\partial\theta/\partial z$. For example, the simulated maxima of $\partial\theta/\partial z$ (Fig. 8) are slightly higher (600, 700, and 600 m for the same dates, respectively) and less intense than those of radiosondes (8, 8, and 18 K km^{-1} , respectively).

5 Perturbed diurnal cycle of the PBL

In the second case study, 20 December 2018, the diurnal cycle of the PBL was perturbed by the sudden arrival of very moist, warm air of oceanic origin. During this warming pe-

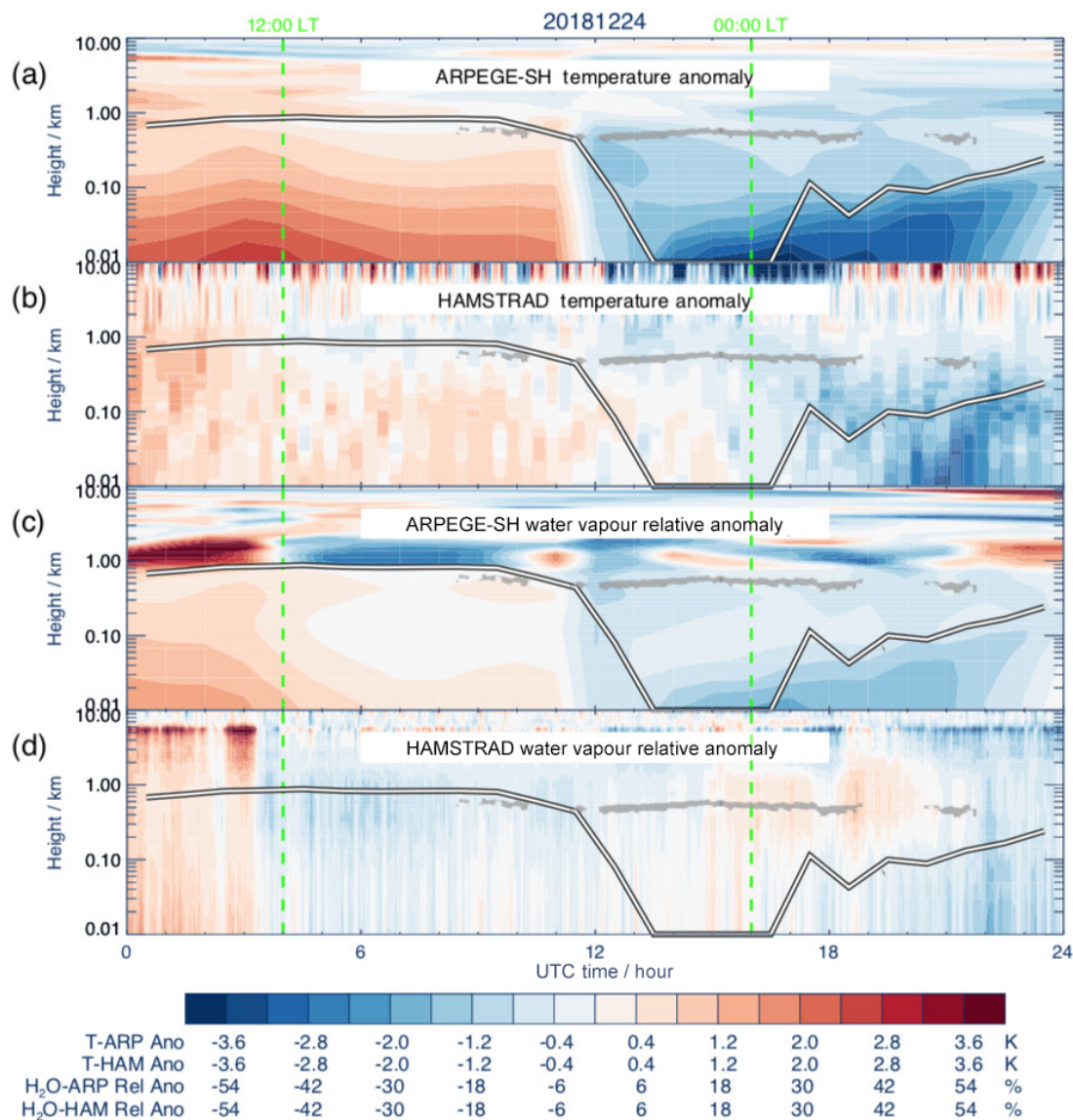


Figure 6. Time–height cross section on 24 December 2018 (UTC time) of (a) the temperature anomaly (K) calculated by ARPEGE-SH and (b) observed by HAMSTRAD, and (c) the water vapour relative anomaly (%) calculated by ARPEGE-SH and (d) observed by HAMSTRAD. Superimposed on all the figures are the SLW cloud altitude (grey area) deduced from the lidar observations (see Fig. 1c) and the top of the planetary boundary layer calculated by the ARPEGE-SH model (black–white thick line). Two vertical green dashed lines indicate 12:00 and 00:00 LT.

riod, the boundary layer remains mixed and does not form a stable boundary layer even when the solar forcing decreases. This will be discussed in detail in Sect. 7.2.

5.1 Clouds

As in Sect. 3.1, the high lidar backscatter ($\beta > 100\beta_{\text{mol}}$) and low depolarization ($< 5\%$) showed the presence of SLW clouds (Fig. 9a, b, and c). Before 13:00 UTC, there is no trace of clouds above Dome C, while from 13:00 to 23:00 UTC SLW clouds are detected between 200 and 600 m. On all panels, we superimposed the PBL top calculated by the

ARPEGE-SH model. We note that the PBL top does not drop to the surface after 12:00 UTC as typically occurs, like on 24 December 2018, but rather remains between 100 and 200 m. Consistent with the conclusions derived from the observations of 24 December 2018, the SLW cloud, once present, stays just above the height of the PBL top.

The cloud fraction, ice water, and liquid water mixing ratios (kg kg^{-1}) calculated by ARPEGE-SH on 20 December 2018 are shown in Fig. 10a, b, and c, respectively. Contrary to the observations, the model simulates mixed-phase clouds (maximum cloud fraction of $\sim 30\%$),

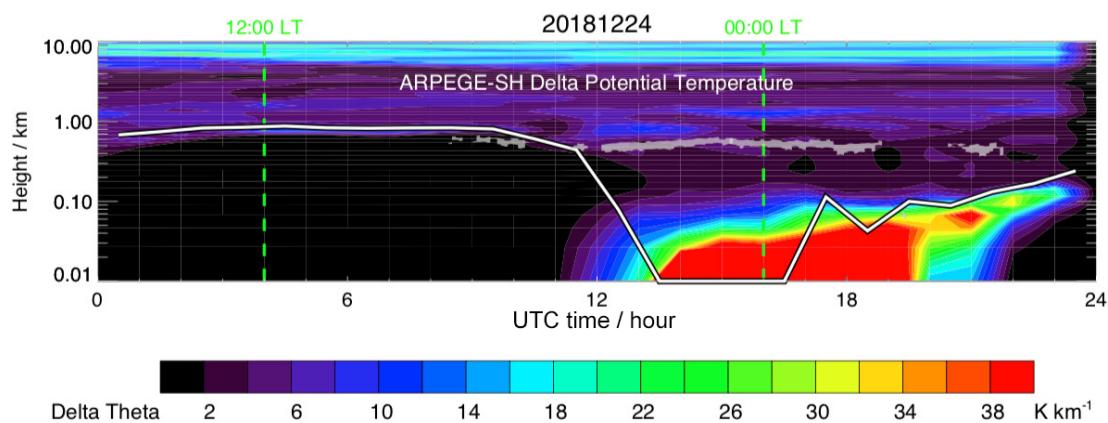


Figure 7. Time–height cross section of $\partial\theta/\partial z$ (K km^{-1}) calculated from ARPEGE-SH temperature on 24 December 2018 (UTC time). Superimposed are the SLW cloud altitude (grey area) deduced from the lidar observations (see Fig. 1) and the top of the planetary boundary layer calculated by the ARPEGE-SH model (black–white thick line). Two vertical green dashed lines indicate 12:00 and 00:00 LT.

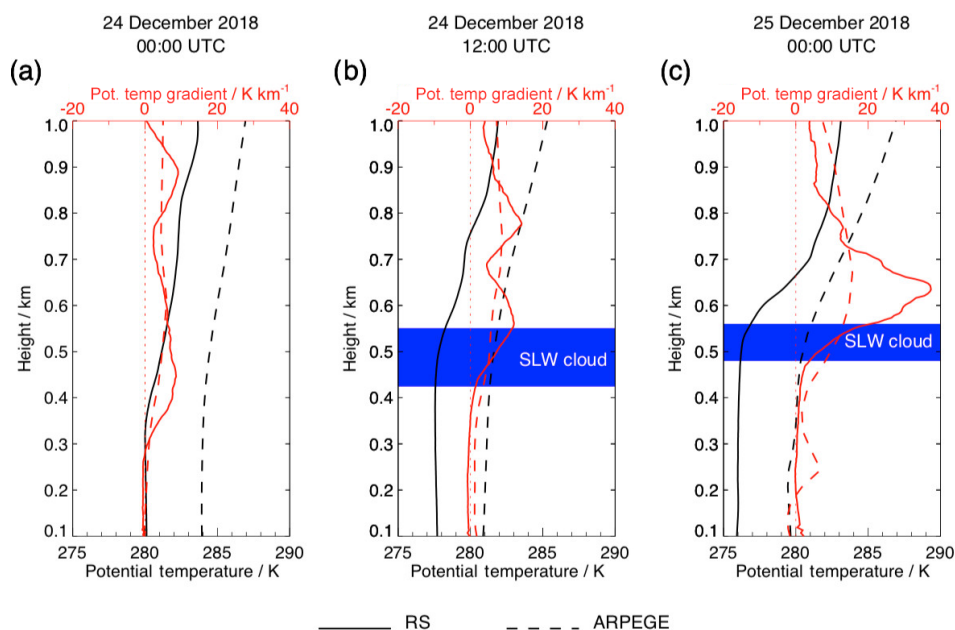


Figure 8. Vertical profiles of potential temperature θ (black) and the gradient in potential temperature $\partial\theta/\partial z$ (red) as calculated from temperature measured by the radiosondes (solid line) and analysed by ARPEGE-SH (dashed line) at Dome C on 24 December 2018 at (a) 00:00 and (b) 12:00 UTC and (c) on 25 December 2018 at 00:00 UTC. The presence and the depth of the SLW cloud detected from lidar observations are indicated by a blue area.

mainly composed of ice, prior to 12:00 UTC; from 00:00 to 06:00 UTC, the clouds are forecasted below the PBL top. After 12:00 UTC, clouds appear 1–2 h later in the model than in the observations, at 14:00–15:00 UTC, just below the PBL top (maximum cloud fraction of $\sim 100\%$). The modelled cloud is mainly composed of ice with some traces of SLW above the PBL around 15:00–16:00 UTC. In all occurrences, the liquid water amounts produced by the model are extremely small and nearly non-existent. We note the presence of high-altitude cirrus (ice) clouds calculated by ARPEGE-SH after 12:00 UTC around 3–4 km height, while they are

not observed likely because the lidar light is attenuated by the SLW layer. As on 24 December 2018, the model fails to reproduce the presence of the SLW layer observed by the lidar near the PBL top.

The diurnal evolutions of the TCI calculated by ARPEGE-SH, the LWP from HAMSTRAD and ARPEGE-SH, and the IWV from HAMSTRAD and ARPEGE-SH on 20 December 2018 are presented in Fig. 11a, b, and c, respectively, with the presence of SLW clouds derived from the lidar observations superimposed on Fig. 11b. Ice clouds are calculated by ARPEGE-SH mainly around 15:00–16:00 UTC, with TCI

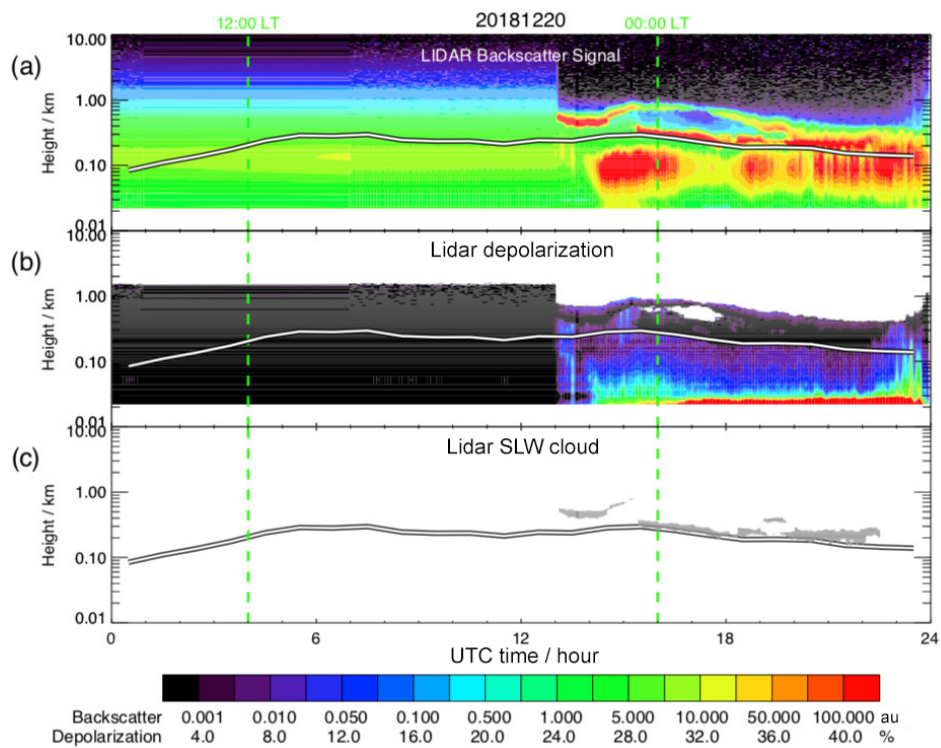


Figure 9. Same as Fig. 2 but for 20 December 2018.

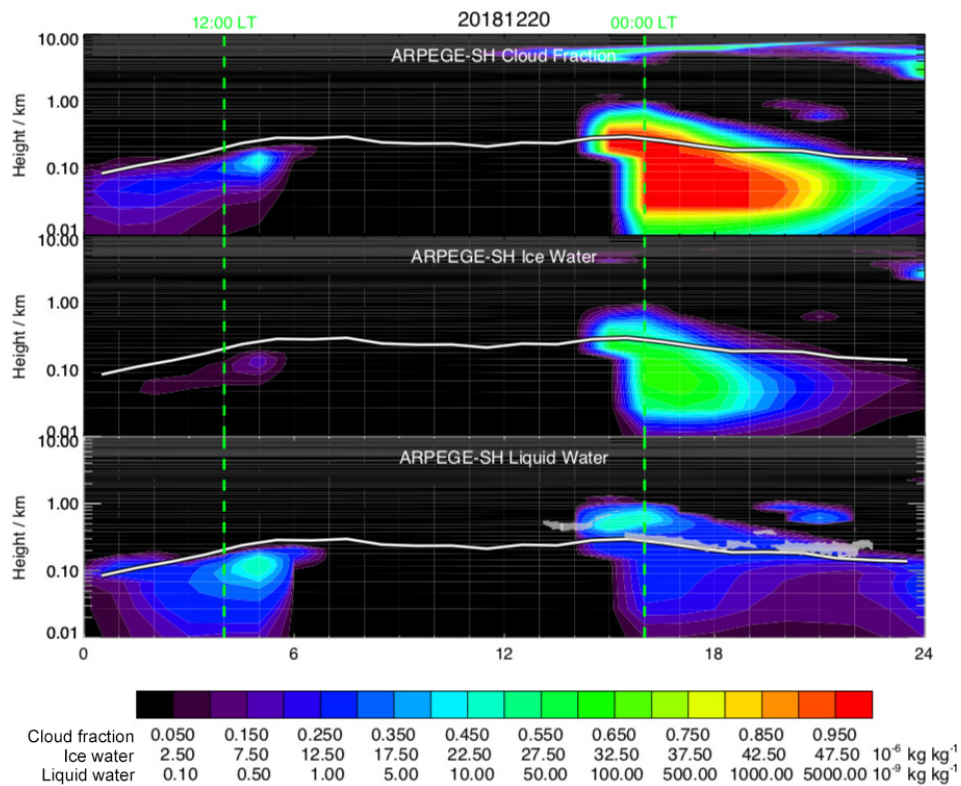


Figure 10. Same as Fig. 3 but for 20 December 2018.

values comparable to those on 24 December 2018. SLW clouds are deduced from HAMSTRAD LWP between 13:00 and 23:00 UTC, which coincides well with the SLW clouds observed by the lidar. The maximum LWP values observed during this episode are much higher ($\sim 50 \text{ g m}^{-2}$) than on 24 December 2018 ($\sim 2\text{--}3 \text{ g m}^{-2}$). Again, the ARPEGE-SH LWP is negligible ($\sim 10^3$ times less than observations). In parallel with the rapid increase in LWP, the observed IWV also jumps from ~ 0.5 to $\sim 2.3 \text{ kg m}^{-2}$ within 1 h after 13:00 UTC. ARPEGE-SH also calculates an increase in IWV but lagged by 1 h and much less intense ($\sim 1.3 \text{ kg m}^{-2}$). Additionally, the model produces a systematically dryer atmosphere compared to HAMSTRAD by about 0.5 kg m^{-2} after 16:00 UTC, although before the cloudy period that starts at 12:00 UTC, ARPEGE-SH and HAMSTRAD IWV are consistent to within $\pm 0.2 \text{ kg m}^{-2}$.

On 20 December 2018, after 13:00 UTC when SLW clouds have been detected at Dome C, both CALIPSO overpasses are far away from Dome C and, for the closest overpass at 13:17 UTC (closest distance to Dome C is 500 km), a very thick ice cloud at about 3 km a.g.l. prevents the lidar radiation from reaching the surface (Fig. S7). Unfortunately, no meaningful information can be ascertained from the spaceborne observations on that day relevant to SLW clouds in the vicinity of Dome C.

5.2 Vertical profiles of temperature and water vapour

The diurnal variations in the temperature and water vapour anomalies on 20 December 2018 as calculated by ARPEGE-SH and measured by HAMSTRAD are shown in Fig. 12. In ARPEGE-SH, a sharp transition between a warm and a cool atmosphere is evident at 12:00 UTC below the top of the PBL. In HAMSTRAD, from 00:00 to 06:00 UTC, the atmosphere starts warming, and then from 06:00 to 13:00 UTC it cools gradually to a minimum. After 13:00 UTC, HAMSTRAD temperatures reveal a warming starting from the surface and progressively thickening until reaching the top of the PBL by the end of the day. Above the PBL, the HAMSTRAD-observed and ARPEGE-SH-calculated temporal evolution of temperature and water vapour are in an overall agreement. In the PBL, the model simulates a moistening around 05:00 UTC, but the most striking event is a sudden drying at 12:00 UTC. In HAMSTRAD, there is a continuous drying from 00:00 UTC, followed by an obvious transition at 13:00 UTC, opposite to that of ARPEGE-SH at 12:00 UTC. The warm and wet atmosphere observed after 13:00 UTC develops a mixed layer, consequently the PBL top no longer collapses to a stable layer, in contrast to what was observed on 24 December. Furthermore, the SLW clouds present in the entrainment zone steadily remain at the PBL top until the end of the day.

5.3 Potential temperature gradient

Figure 13 shows $\partial\theta/\partial z$ (K km^{-1}) from ARPEGE-SH, with the evolution of the PBL top and the SLW cloud superimposed. In these perturbed conditions, the SLW clouds are present a few tens of metres above the top of the PBL after 12:00 UTC. The PBL top is located in a layer coinciding with the local maximum of $\partial\theta/\partial z$, around 100–300 m, and does not dramatically decrease to the surface for the rest of the day.

Figure 14a, b, and c show the vertical profiles of θ (K) and $\partial\theta/\partial z$ (K km^{-1}) as calculated from temperature measured by the radiosondes and analysed by ARPEGE-SH at Dome C on 20 December 2018 at 00:00 and 12:00 UTC and on 21 December 2018 at 00:00 UTC, respectively. The presence and the depth of the SLW cloud detected from lidar observations are highlighted in the figure. The ARPEGE-SH profiles are about 0–5 K warmer than the observations. From 50 m upward, the maximum of $\partial\theta/\partial z$ is measured at 75, 150, and 375 m on 20 December 2018 at 00:00 and 12:00 UTC and on 21 December 2018 at 00:00 UTC, with a corresponding amplitude of 75, 40, and 55 K km^{-1} . The location of the observed maximum in the potential temperature gradient is consistent with the ARPEGE-SH calculations on 20 December 2018 prior to the warm and wet episode: at 00:00 UTC (Fig. 14a), the calculated $\partial\theta/\partial z$ is maximum at 75 m and reaches 100 K km^{-1} . However, at 12:00 UTC (Fig. 14b) the modelled $\partial\theta/\partial z$ peaks at 200 m (slightly higher than observed) with a value of 50 K km^{-1} . On the following day at 00:00 UTC (Fig. 14c), $\partial\theta/\partial z$ calculated by ARPEGE-SH shows two maxima at 100 and 450 m with an amplitude of 45 and 25 K km^{-1} , respectively, while the observations demonstrate a single maximum just below 400 m.

6 Impact of SLW clouds on net surface radiation

The presence of clouds over Dome C has a strong impact on the net surface radiation as demonstrated by Ricaud et al. (2017). This can be seen clearly in the time series of upwelling and downwelling longwave and shortwave fluxes observed by BSRN for the two case studies.

6.1 Typical PBL case – 24 December 2018

Figure 15 (top panel) shows the time evolution of the net surface radiation as measured by the BSRN instruments and as calculated by ARPEGE-SH on 24 December 2018, superimposed on SLW cloud height. We also show the time evolution of the difference between surface radiation (W m^{-2}) observed by BSRN and calculated by ARPEGE-SH on 24 December 2018, in longwave downward ($\text{LW}\downarrow$), longwave upward ($\text{LW}\uparrow$), shortwave downward ($\text{SW}\downarrow$), and shortwave upward ($\text{SW}\uparrow$) components, superimposed on LWP (Fig. 15, middle panel). We highlight four periods with images taken from the webcam installed on the shelter hosting

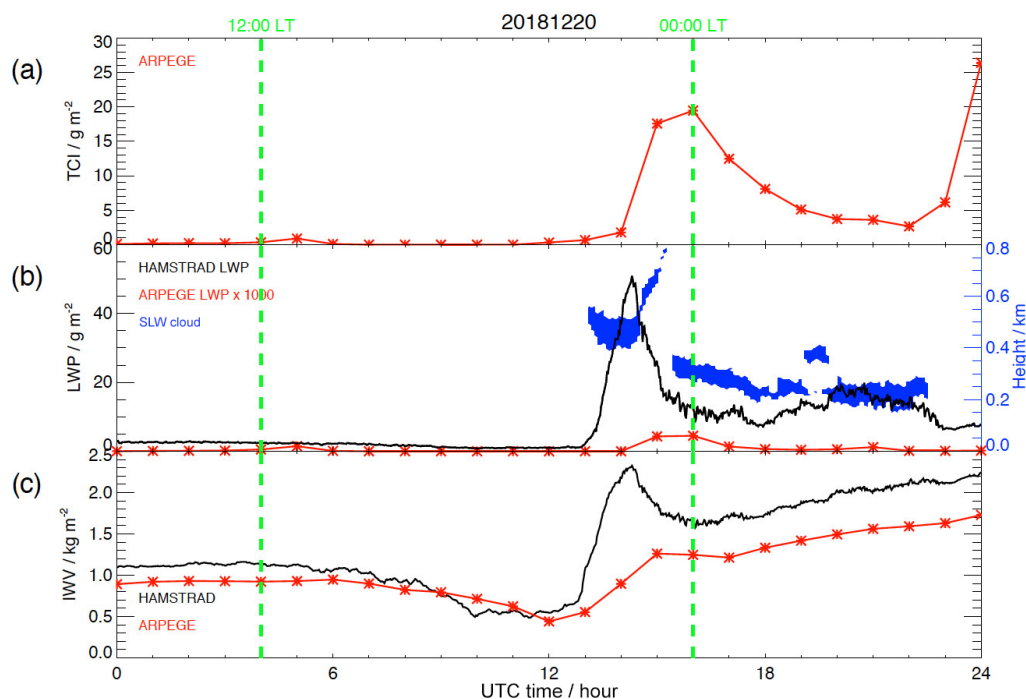


Figure 11. Same as Fig. 4 but for 20 December 2018.

the lidar and HAMSTRAD (Fig. 15, bottom panel): (a) at 00:25 UTC (cirrus clouds, no SLW cloud), (b) at 03:56 UTC (cirrus clouds, no SLW cloud), (c) at 09:46 UTC (SLW cloud), and (d) at 17:20 UTC (SLW cloud). The net surface radiation shows maxima between 00:00 and 05:00 UTC (08:00–13:00 LT) and minima between 11:00 and 13:00 UTC (19:00–21:00 LT) in the ARPEGE-SH and BSRN time series. When SLW clouds are present in the observations (08:00–10:00, 12:00–19:00, and around 21:00 UTC), whilst absent in ARPEGE-SH, the measured net surface radiation is systematically greater by 20–30 W m^{-2} than the simulated one. In the presence of SLW clouds after 12:00 UTC, this difference is mainly attributable to the $\text{LW}\downarrow$ component, BSRN values being 50 W m^{-2} greater than those of ARPEGE-SH. Thus, SLW clouds tend to radiate more LW radiation toward the ground (like greenhouse gases) than more transparent clouds, like cirrus, do. There are differences from -30 to $+60 \text{ W m}^{-2}$ between observed and calculated $\text{SW}\downarrow$ and $\text{SW}\uparrow$ components, but this difference falls within $\pm 10 \text{ W m}^{-2}$ for the net SW surface radiation ($\text{SW}\downarrow - \text{SW}\uparrow$). The reflective impact of SLW layers can also be seen after 12:00 UTC: unlike observed SLW clouds, ARPEGE-SH simulates ice clouds and therefore $\text{SW}\downarrow$ values that are too high. The difference between observed and simulated values of this parameter thus increases, as can be seen in the figure. But because of the high values in surface albedo, a compensating effect occurs in the surface-reflected SW fluxes, and the resulting impact on net radiation is quite weak (the time series of the observed–simulated difference in incoming and

reflected SW flux follow each other quite well). The major impact on net radiation is therefore related to the longwave fluxes.

6.2 Perturbed PBL case – 20 December 2018

Figure 16 (top panel) shows the net surface radiation as measured by the BSRN photometric instruments and as calculated by ARPEGE-SH for 20 December 2018, superimposed on the SLW clouds. We also show the time evolution of difference in surface radiation (W m^{-2}) observed by BSRN and calculated by ARPEGE-SH on 20 December 2018 for $\text{LW}\downarrow$, $\text{LW}\uparrow$, $\text{SW}\downarrow$, and $\text{SW}\uparrow$ components, superimposed on LWP (Fig. 16, middle panel). We highlight four periods with snapshots taken from the webcam (Fig. 16, bottom panels): (a) 07:15 UTC (clear sky), (b) 12:35 UTC (clear sky), (c) 13:30 UTC (SLW cloud), and (d) 21:00 UTC (SLW cloud). Before 13:00 UTC, there are no clouds above Dome C, whilst after 13:00 UTC clouds are present. The diurnal evolution of the modelled and observed net surface radiation shows a maximum of $\sim +50 \text{ W m}^{-2}$ in ARPEGE-SH and $\sim +85 \text{ W m}^{-2}$ in BSRN over the period 00:00–04:00 UTC and a minimum of about -50 W m^{-2} around 12:00–13:00 UTC in both time series. Nevertheless, when SLW clouds are observed at 13:00 UTC, the observed net surface radiation jumps to $+10 \text{ W m}^{-2}$, a feature not reproduced in the model. The difference between the BSRN-observed and ARPEGE-SH-modelled net surface radiation is larger than $+30 \text{ W m}^{-2}$ when SLW clouds are present, reaching $+60 \text{ W m}^{-2}$ when the LWP measured by HAMSTRAD is

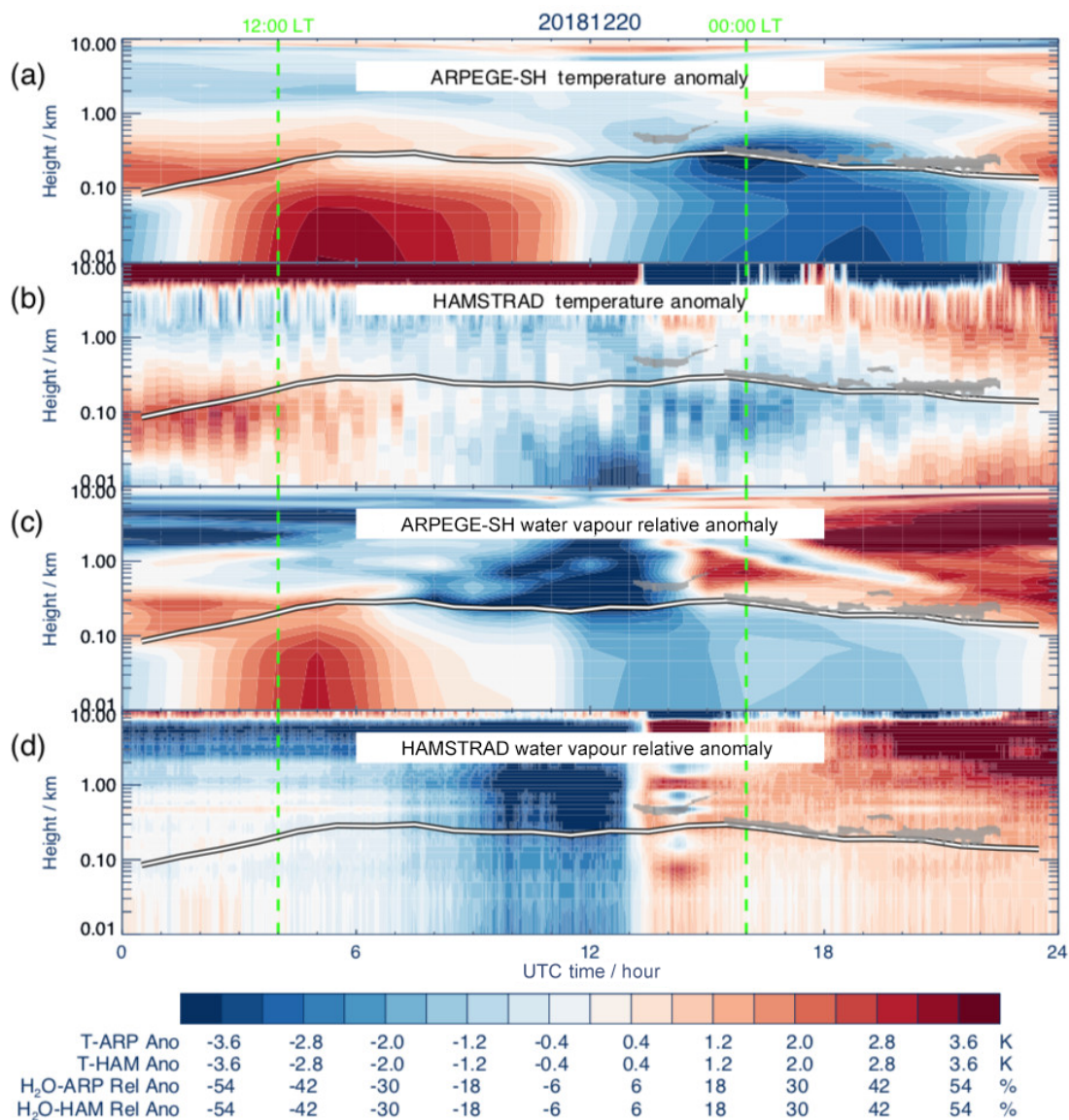


Figure 12. Same as Fig. 6 but for 20 December 2018.

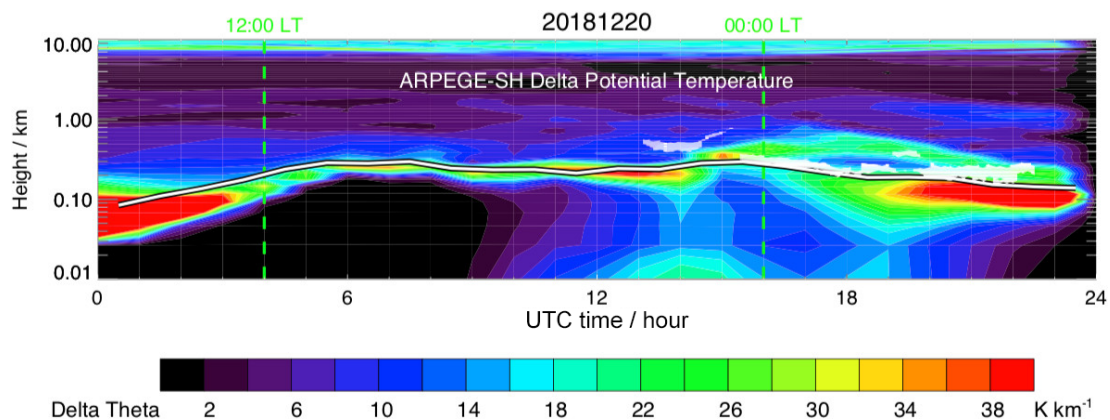


Figure 13. Same as Fig. 7 but for 20 December 2018.

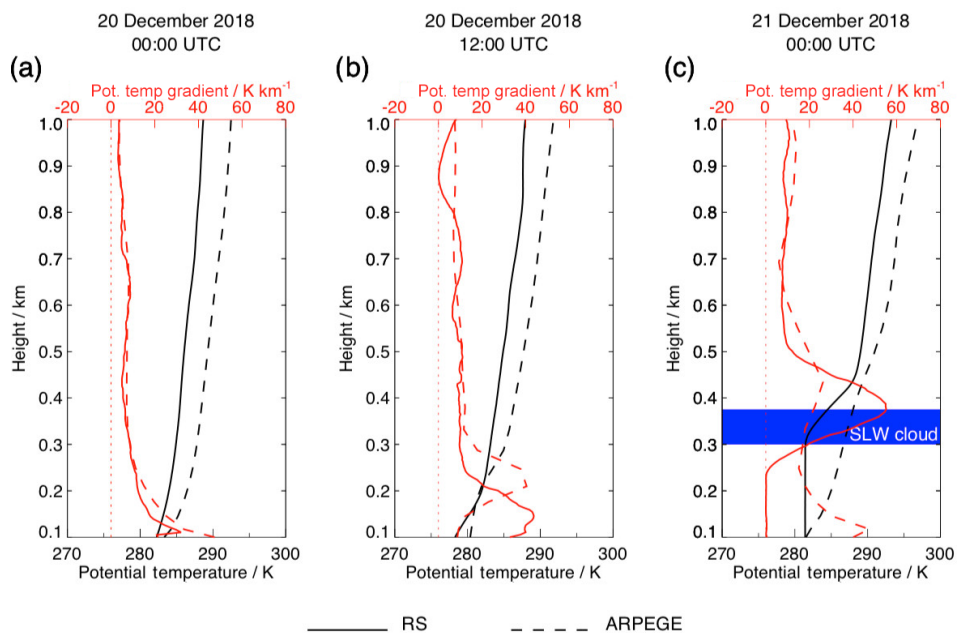


Figure 14. Same as Fig. 8 but on 20 December 2018 at (a) 00:00 and (b) 12:00 UTC and (c) on 21 December 2018 at 00:00 UTC.

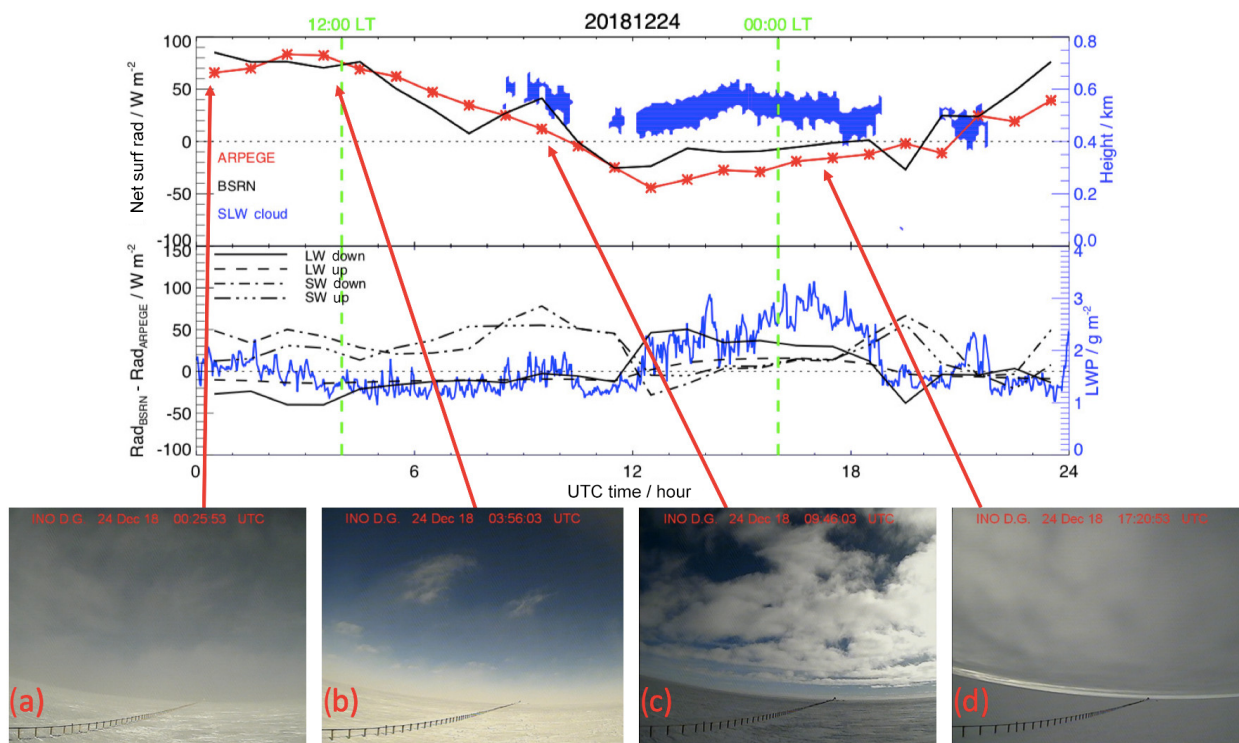


Figure 15. Top: diurnal variation in the net surface radiation (W m^{-2}) observed by BSRN (black solid line) and calculated by ARPEGE-SH (red crossed line) on 24 December 2018 in UTC time. Superimposed is the SLW cloud height (blue) deduced from the lidar. Middle: diurnal variation in the difference between surface radiation (W m^{-2}) observed by BSRN and calculated by ARPEGE-SH on 24 December 2018 for longwave downward (black solid), longwave upward (black dashed), shortwave downward (black dashed dotted), and shortwave upward (black dashed triple dotted) components. Superimposed is LWP (blue) measured by HAMSTRAD. Bottom: four webcam images show the cloud coverage at (a) 00:25 UTC and (b) 03:56 UTC (cirrus clouds, no SLW cloud), (c) 09:46 UTC (SLW cloud), and (d) 17:20 UTC (SLW cloud). Two vertical green dashed lines indicate 12:00 and 00:00 LT.

at its maximum (50 g m^{-2} at 13:00 UTC). This is twice the difference observed in the non-perturbed PBL episode detailed in Sect. 3.4. This underlines again the strong impact SLW clouds may have on the radiation budget over Antarctica. In the presence of SLW clouds after 13:00 UTC, the difference in net surface radiation is mainly attributable to the $\text{LW}\downarrow$ component, BSRN values being 100 W m^{-2} greater than those of ARPEGE-SH. The $\text{SW}\downarrow$ and $\text{SW}\uparrow$ also decrease due to the high reflectivity of the SLW layer seen at 12:00 and again at 15:00 UTC. Note that there are differences from -100 to $+60 \text{ W m}^{-2}$ between observed and calculated $\text{SW}\downarrow$ and $\text{SW}\uparrow$ components, but this difference falls below 20 W m^{-2} for the net SW surface radiation ($\text{SW}\downarrow - \text{SW}\uparrow$). Both SW components decrease after 17:00 UTC. Some of this may be due to (1) increasing LWP and (2) the presence of precipitating ice crystals and/or blowing snow (characterized by red spots in Fig. 9b) that are increasing optical depth and decreasing transmission or visibility (webcam images in Fig. 16d) although surface wind was rather weak ($3\text{--}10 \text{ m s}^{-1}$, not shown).

7 Discussions

7.1 SLW clouds vs. mixed-phase clouds

In order to evaluate whether the observed cloud is constituted of liquid and/or mixed-phase water, we have considered the raw signals recorded by the lidar. For the two dates under consideration (Figs. S8 and S9 relative to 24 and 20 December 2018, respectively), we have represented (top) the P signal as the signal received with the same polarization as the laser (unpolarized component). Any suspended object can contribute to P signal. We have also represented the S (cross-polarized) lidar signal (bottom) that is only produced by non-spherical (obviously frozen at Dome C) particles and, to a smaller extent, by multiple scattering in water clouds.

First of all, an elevated P signal above $\sim 400 \text{ m}$ on 24 December 2018 ($P \geq 0.1 \text{ mV}$) and above $\sim 200 \text{ m}$ on 20 December 2018 ($P \geq 0.3 \text{ mV}$) is associated with a cloud as shown in Sects. 4.1 and 5.1. Inside these clouds, the S signal is always very low: $S \sim 0.003 \text{ mV}$ on 24 December 2018 and $\sim 0.01 \text{ mV}$ on 20 December 2018. Consequently, the S signal is very weak and corresponds to a maximum of $\sim 3\%$ of the corresponding P signal. Some S signal is nevertheless present in the cloud and could be given by multiple scattering inside the truly liquid water cloud and/or the effective presence of ice particles.

When considering the lidar depolarization diurnal evolutions presented in Figs. 2b and 9b associated with the two dates, ice particles could have disappeared in the low depolarization ratio S/P of the SLW layer because the P signal inside the SLW cloud is very high compared to the S signal. But when considering the P and S signals distinctively (Figs. S8 and S9), the S signal remains very weak in the SLW

cloud compared to the P signal, whatever the date considered. Consequently, even if the presence of some ice particles scattered within the SLW layers cannot be excluded from the S signal plot, the very low depolarization of the layers leads us to classify them as a liquid cloud.

The important point is that the optical properties of the layer, relevant for the radiative budget in the shortwave, such as optical extinction, optical depth, and asymmetry factors, are bound to the P signal, being, e.g., optical extinction in the visible proportional to the lidar P signal. Thus, the shortwave radiative characteristics of the cloud are driven by the P signal and thus by liquid water.

On the other hand, when we consider the aerosol depolarization ratio measured by the lidar (Fig. 2b) and the total snow flux calculated by ARPEGE-SH (Fig. S2) on 24 December 2018, it is obvious that solid precipitation is present from 00:00 to 10:00 UTC in a layer from $\sim 500 \text{ m}$ to the surface (vertical stripes). Therefore, physical processes are occurring within the cloud to deplete liquid and turn it into solid, causing the ice observed and calculated below the SLW layer. In this case, the ice microphysics would also be important since they lead to the termination of the SLW layer, hence indirectly impacting the radiative budget. As a consequence, we cannot completely rule out the possibility that this is an SLW layer of an overall mixed-phase cloud.

7.2 SLW clouds and PBL

During the YOPP SOP-SH, SLW clouds were observed in the lidar data for 15 d in December (49 % of days) and 13 d in January (47 %), which is a similar rate of occurrence to other years (53 % in December 2016 and 2018; 51 % in January 2018 and 2019) (Fig. 17). A day is flagged with an SLW cloud occurrence when an SLW cloud has been detected in the lidar observations for a period longer than 1 h. The clouds observed during the SOP-SH are typically located at the top of the PBL (100 to 400 m height) and are 50–100 m thick.

The presence of SLW clouds in the atmosphere is strongly dependent on the temperature field. From Fig. 2.33 of Pruppacher and Klett (2012), the percentage of clouds containing no ice becomes non-negligible at temperatures greater than -35°C , although SLW clouds have been observed at lower temperatures over Russia (-36°C) and the Rocky Mountains in the USA (-40.7°C). Recent laboratory measurements show that liquid water can exist down to -42.55°C (Goy et al., 2018).

Considering that the SLW clouds at Dome C are so thin, they resemble stratocumulus, as can be observed at middle latitudes. The diurnal cycle of the SLW cloud also evokes that of oceanic stratocumulus, with a trend to fragmentation and/or dissipation during the “day” (local noon) because of solar absorption and to a solid deck state during the “night” (local midnight) because of reversed buoyancy due to cloud top longwave cooling. We use the terms night and day here for convenience, though solar radiation remains positive 24 h

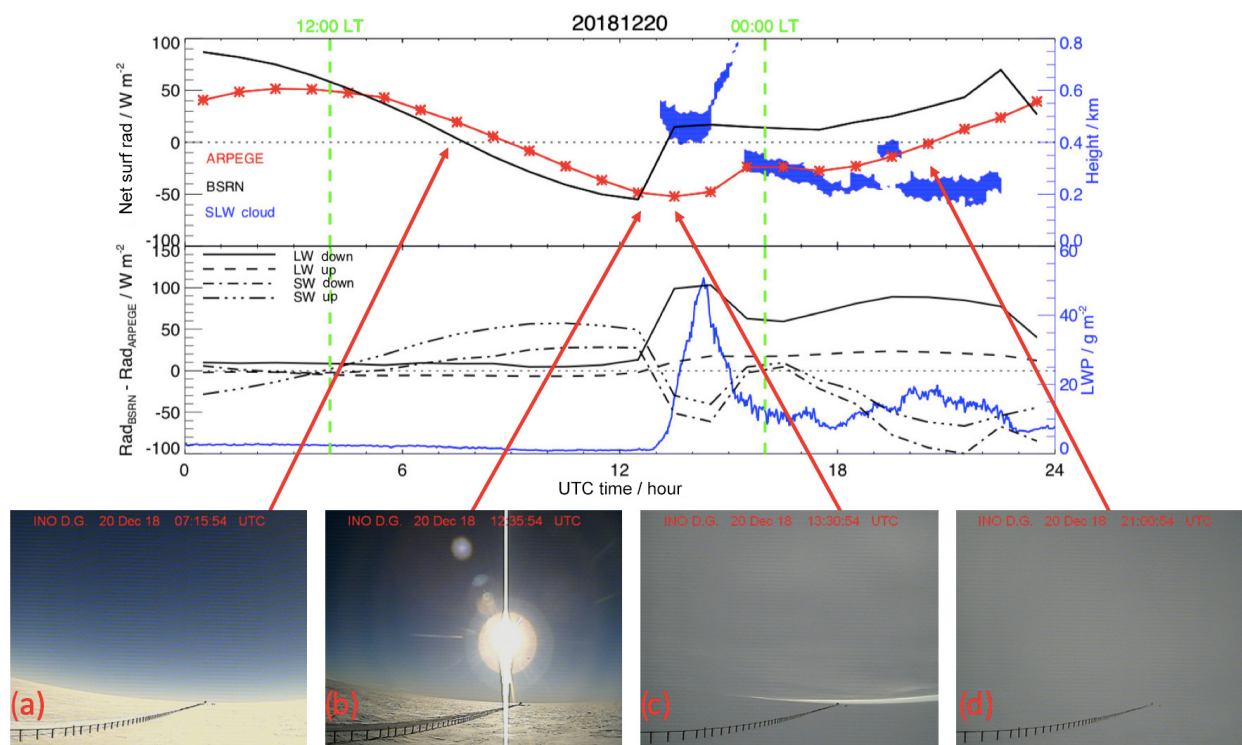


Figure 16. Same as Fig. 15 but for 20 December 2018, whilst the four webcam images were selected at (a) 07:15 and (b) 12:35 UTC (clear sky), (c) 13:30, and (d) 21:00 UTC (SLW cloud).

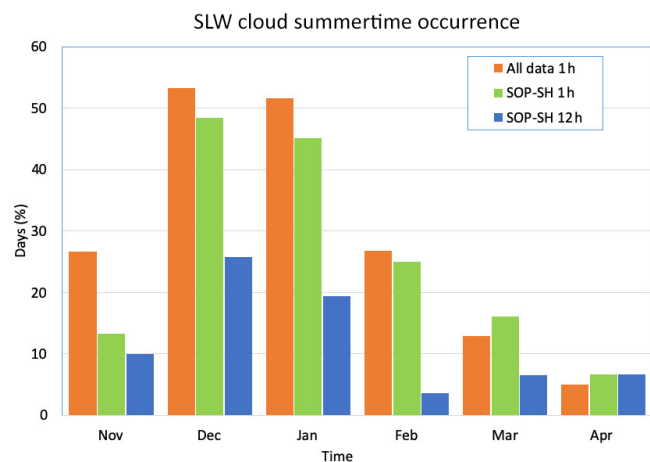


Figure 17. Percentage of days per month that SLW clouds were detected within the lidar data for more than 1 h per day over different summer periods: “All data 1h” (orange) refers to November (2016–2018), December (2016–2018), January (2018–2019), February (2018–2019), and March (2018–2019); “SOP-SH 1h” (green) represents the YOPP campaign (November 2018 to April 2019). “SOP-SH 12h” (blue) represents the percentage of days per month that SLW clouds were detected during the YOPP campaign within the lidar data for more than 12 h per day.

long at this period of the year. During the SOP-SH, SLW clouds were observed in the lidar data for approximately 48 % of days (Fig. 17), but it is not yet evident whether they were formed during the day (local noon) when the mixed layer becomes thick enough to reach the condensation level, and vertically broadened during the night or created during the night (local midnight) and then dissipated during the coming day. Complementary observations would be needed, in particular turbulence profiles from the surface to above the top of boundary-layer clouds, to determine what is the coupling–decoupling diurnal cycle of these clouds.

The diurnal evolution of the top of the PBL is consistent with previous studies carried out at Dome C (e.g. Argentini et al., 2005; King et al., 2006; Ricaud et al., 2012; Casasanta et al., 2014), with a top higher when there is a relatively warm mixed layer than in colder stable conditions.

The collocation of the positive potential temperature gradient with the height of the SLW clouds is consistent with the schematic representation of the diurnal variation in the PBL illustrated by Stull (2012) and adapted by Ricaud et al. (2012) for the Eastern Antarctic Plateau. Figure 18 is a modified version of Fig. 12 from Ricaud et al. (2012) to take into account the impact of the clouds on the PBL structure. Starting with the simplest, cloud-free case, we have during the convective (mixing) period a mixed layer at the top of which is located the “entrainment zone”, so-named because air parcels coming from the above free troposphere are en-

trained into the mixed layer below under the effect of overshooting thermals and compensating for descending currents. When clouds form at the top of the PBL (boundary-layer clouds), we consider that the PBL locally (i.e. where clouds are present) extends to the top of these clouds. The PBL is clearly separated from the above stable free troposphere by the so-called “capping inversion”. The cloud layers as well as the capping inversion zone are thin, of the order of 100 m. When the stable layer forms close to the surface, the SLW cloud may persist over the residual mixed layer, as may the capping inversion zone, which can also be qualified as “residual”. The stable layer is then progressively eroded, when the incoming available energy becomes large enough to ensure turbulent mixing from the surface. The new mixing layer thus grows through the previous stable layer and residual mixed layer, until it reaches the residual capping inversion. The stratification of the different layers is characterized by the simplified potential temperature profiles in Fig. 18. Considering both the potential temperature gradients and the vertical extent of the SLW cloud, these layers are quite thin, less than 100 m deep.

7.3 SLW clouds in ARPEGE-SH

In comparison with observations, ARPEGE-SH consistently underestimates LWP by several orders of magnitude. This is due in part to the partitioning into liquid and ice phases in the model, which is a simple function of temperature such that, below -20°C , all cloud particles are iced. The inability of ARPEGE-SH to reproduce the observed liquid water content of the cloud leads to an underestimate of the simulated downwelling longwave radiation relative to observations and an overestimate of both upwelling and downwelling shortwave flux. This effect is particularly notable in the perturbed PBL case study where the high moisture content leads to an enhanced longwave effect. As the SLW cloud horizontal extent in the first case study is between ~ 450 and ~ 700 km and persists over more than 12 h (Sect. 4.1), the discrepancy in the net surface radiation between observation and NWP model may have a strong impact on the calculation of the radiation budget over Antarctica. Lawson and Gettelman (2014) showed that better representation of liquid water in modelled mixed-phase clouds in global climate models led to an increase of 7.4 W m^{-2} in the cloud radiative effect over Antarctica.

In Fig. 17, we show the percentage of days per month that SLW clouds were detected within the lidar data for more than 12 h per day (blue) during SOP-SH. As expected, SLW clouds with a minimum duration of 12 h (blue) occur less often than SLW clouds with a minimum duration of 1 h (green). But whatever the criterion used (1 h or 12 h), the maxima of SLW cloud presence occur in December and January during SOP-SH. Twelve-hour SLW clouds occurred about a quarter of the days (20 %–25 %) compared to roughly half of the days for 1 h SLW clouds (40 %–45 %). This reinforces

the argument of the critical importance of representing SLW clouds well in models in order to better estimate radiation budget over Antarctica.

Furthermore, even when considering analyses of ARPEGE-SH at 00:00, 06:00, 12:00, and 18:00 UTC and associated forecasts (not shown), neither IWV nor LWP are significantly modified, and SLW remains underestimated. The 4Dvar analysis is not able to correct the dry bias especially during the case of 20 December 2018 probably because it is influenced by large-scale advection. The underestimation of the SLW in ARPEGE-SH can be explained by the fact that (1) the underestimation of liquid water is mainly a physical problem in the model related to the ice–liquid partition function vs. temperature (see below) and (2) since the cloud water is not a model control variable in the 4DVar scheme, it cannot be updated by the analysis step of the 4DVar data assimilation process.

We have thus tried to modify the ice partition function (ice or liquid water vs. temperature) used in the ARPEGE-SH operational model (Fig. S10). We noticed that, for temperatures below -20°C , water was present only in the solid form in the model. A test has been performed for 20 and 24 December 2018 with ARPEGE-SH by considering a new ice partition function allowing the presence of liquid water for temperature between -20 and -40°C (Fig. S10). The analyses were done at 00:00 UTC and the forecasts from 01:00 to 24:00 UTC. This run was labelled as ARPEGE-SH-TEST.

For 24 December 2018, and consistently with Fig. 3, we have drawn in Fig. S11 the diurnal evolutions of different variables calculated by ARPEGE-SH-TEST: (a) the cloud fraction, (b) the ice water mixing ratio, and (c) the liquid water mixing ratio. Similarly, and consistently with Fig. 4, Fig. 19 presents (a) the ARPEGE-SH-TEST TCI, (b) the LWP measured by HAMSTRAD and calculated by ARPEGE-SH-TEST, and (c) the IWV measured by HAMSTRAD and calculated by ARPEGE-SH-TEST. Eventually, and consistently with Fig. 9, Fig. S13 presents the net surface radiation observed by BSRN and calculated by ARPEGE-SH-TEST and the difference between surface radiation of longwave downward, longwave upward, shortwave downward, and shortwave upward components observed by BSRN and calculated by ARPEGE-SH-TEST. In the same manner, for the case of 20 December 2018, Figs. S12, 20, and S14 echo Figs. 11, 12, and 16, respectively.

On 24 December 2018 (typical case), the new partition function significantly improves the modelled SLW, with liquid water content about 1000 times greater in ARPEGE-SH-TEST than in ARPEGE-SH and LWP varying from ~ 0 to $\sim 3\text{ g m}^{-2}$ consistently with HAMSTRAD to within $\pm 0.5\text{ g m}^{-2}$. The impact on the net surface radiation is obvious with an excellent agreement between ARPEGE-SH-TEST and BSRN to within $\pm 20\text{ W m}^{-2}$. Unfortunately, on 20 December 2018 (perturbed case), even if the impact on SLW clouds is important (liquid water content multiplied by a factor of 100), LWP is still a factor of 10 less in ARPEGE-

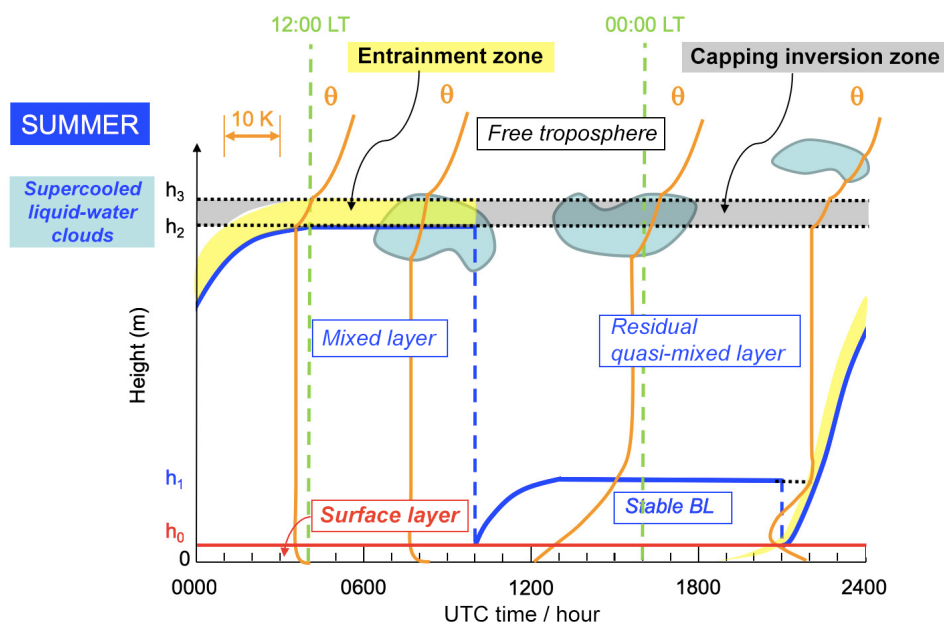


Figure 18. Figure modified and updated from Fig. 12 of Ricaud et al. (2012) showing the diurnal evolution (UTC time) of the different layers in the planetary boundary layer (PBL) with h_0 the top of the surface layer, h_3 the daily overall top of the PBL, and h_1 the top of the intermediate stable layer within the PBL. The orange lines symbolize the vertical profiles of potential temperature θ and the light blue areas the SLW clouds. The layer between h_2 and h_3 is named “capping inversion zone”. The yellow area represents the “entrainment zone” at the top of the (cloudy or cloud-free) mixed layer. When the mixed layer is fully developed, the entrainment zone coincides with the capping inversion zone. Note that LT = UTC + 8 h, midnight and noon in the local time reference being indicated by the green dashed lines.

SH-TEST than in HAMSTRAD. ARPEGE-SH-TEST still fails to reproduce the large increase in liquid water and IWV at 13:00 UTC since the local maximum is calculated 2 h later. The impact on the net surface radiation is weak, with ARPEGE-SH-TEST underestimating the net surface radiation by 50 W m^{-2} compared to observations, mainly attributable to the downwelling longwave surface radiation from BSRN being 100 W m^{-2} greater than that of ARPEGE-SH-TEST.

Finally, the bias on the net surface radiation and the underestimation of IWV and LWP of the model compared to the observations is strongly reduced when using a new ice partition function in ARPEGE-SH-TEST. This suggests that LWP has more impact than IWV on $\text{LW}\downarrow$ due to the small quantities of specific humidity at Dome C.

8 Conclusions

A comprehensive water budget study was performed during the Year of Polar Prediction (YOPP) SOP-SH at Dome C (Concordia, Antarctica) from mid-November 2018 to mid-February 2019. Supercooled liquid water (SLW) clouds were observed and analysed by means of remote-sensing ground-based instrumentation (tropospheric depolarization lidar, HAMSTRAD microwave radiometer, BSRN net surface radiation), radiosondes, spaceborne sensor (CALIOP/CALIPSO depolarization lidar), and the NWP

ARPEGE-SH. The analysis shows that SLW clouds were present from November to March, with the greatest frequency occurring in December and January since $\sim 50\%$ of the days in summer time exhibited SLW clouds for at least 1 h. The clouds observed during the SOP-SH are typically located at the top of the boundary layer (100 to 400 m height) and are 50–100 m thick.

The analyses focused on two periods showing (1) a typical diurnal cycle of the PBL on 24 December 2018 (warm and dry, local mixing layer followed by a thinner cold and dry, local stable layer which develops when the surface has cooled down) and (2) a perturbed diurnal cycle of the PBL on 20 December 2018 (a warm and wet episode prevented by a clear diurnal cycle of the PBL top). In both cases thin (~ 100 m thick) SLW clouds have been observed by ground-based and spaceborne lidars developing within the entrainment and the capping inversion zones at the top of the PBL. Spaceborne lidar observations revealed horizontal extensions of these clouds as large as 700 km for the 24 December case study. ARPEGE-SH was not able to correctly estimate the ratio between liquid and solid water inside the cloudy layers, with LWP always strongly underestimated by a factor of 1000 in the studied cases, mainly because the liquid–ice partition function used in the model favours ice at temperatures less than -20°C . Consequently, the net surface radiation was affected by the presence of SLW clouds during these two episodes. The net surface radiation observed by BSRN

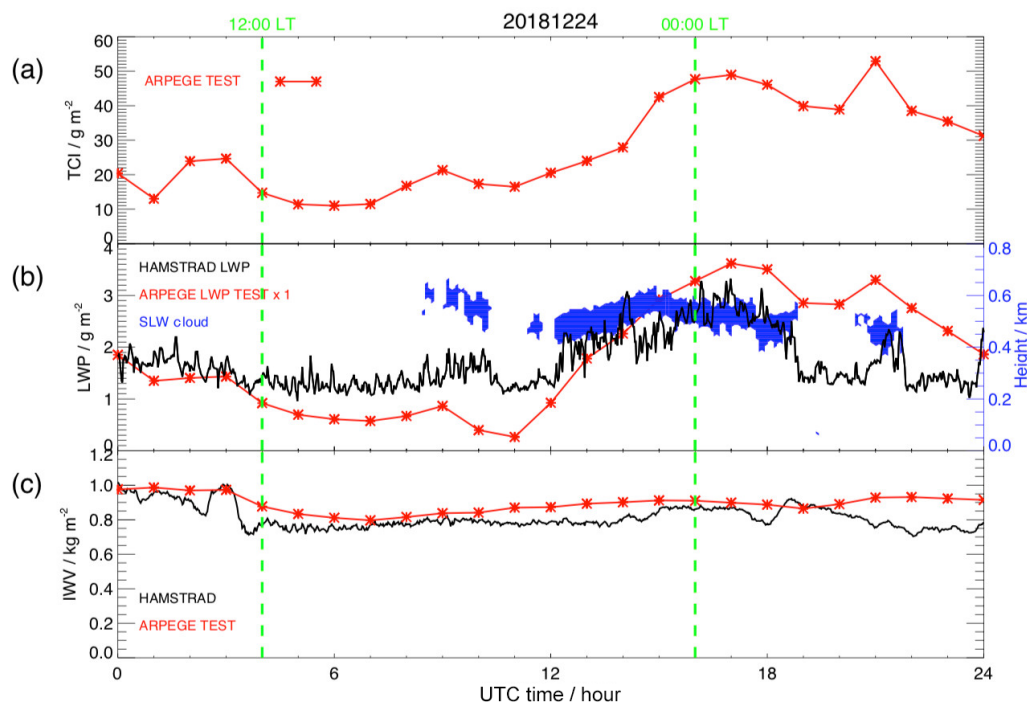


Figure 19. Diurnal variation on 24 December 2018 (UTC time) of (a) the total column of ice (TCI) (g m^{-2}) calculated by ARPEGE-SH in test mode (red crossed line), (b) the liquid water path (LWP) measured by HAMSTRAD (g m^{-2} , black solid line) and calculated by ARPEGE-SH in test mode (– no scaling – g m^{-2} , red crossed line), and (c) the integrated water vapour (IWV, kg m^{-2}) measured by HAMSTRAD (black solid line) and calculated by ARPEGE-SH in test mode (red crossed line). Superimposed on panel (b) is the SLW cloud thickness (blue area) deduced from the lidar observations (see Fig. 2c) (blue y axis on the right of the figure). Two vertical green dashed lines indicate 12:00 and 00:00 LT.

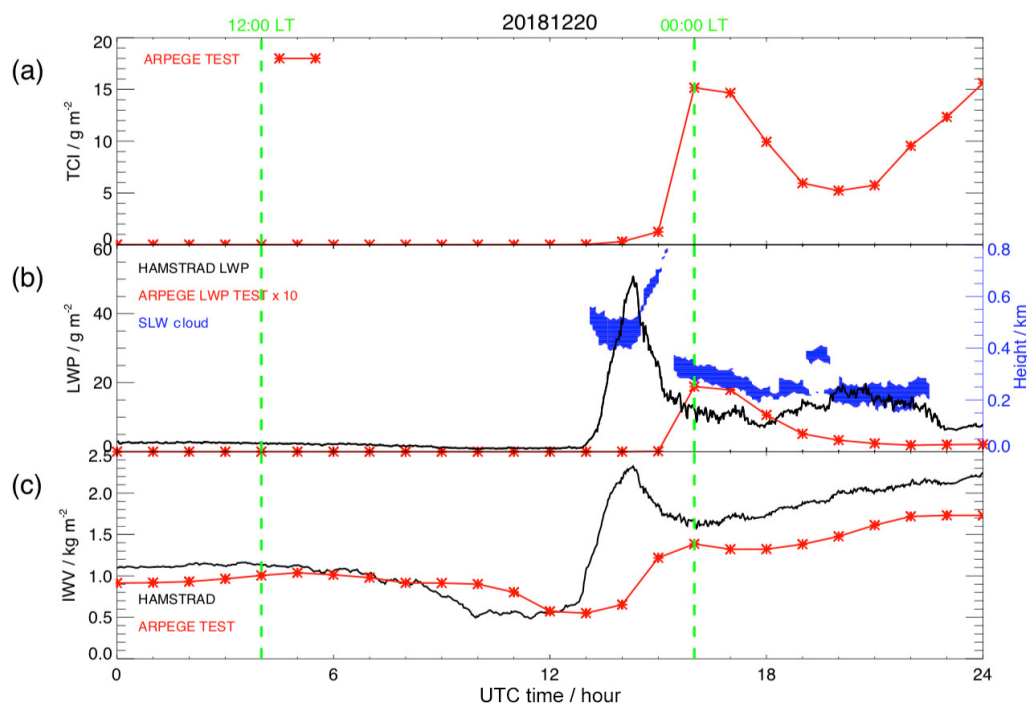


Figure 20. Same as Fig. 19 but on 20 December 2018 (UTC time), and LWP from ARPEGE-SH in test mode has been multiplied by a factor of 10.

was 20–30 W m⁻² higher than that modelled in ARPEGE-SH on 24 December 2018 (typical diurnal cycle of the PBL), this difference reaching +50 W m⁻² on 20 December 2018 (perturbed diurnal cycle of the PBL), consistent with the total observed liquid water being 20 times greater in the perturbed PBL diurnal cycle than in the typical PBL diurnal cycle. The difference in the net surface radiation is mainly attributable to longwave downward surface radiation, with BSRN values being 50 and 100 W m⁻² greater than those of ARPEGE-SH in the typical and perturbed cases, respectively.

The ice–liquid partition function used in the ARPEGE-SH NWP has been modified to favour liquid water at temperatures below -20 down to -40 °C. For the two study cases, the model run with this new partition function has been able to generate SLW clouds. During the typical case, modelled LWP was consistent with observations and, consequently, the net surface radiation calculated by the model agreed with measurements to within ±20 W m⁻². During the perturbed case, modelled LWP was a factor of 10 less than observations and, consequently, the model underestimated the net surface radiation by ~50 W m⁻² compared to observations.

Time coincident ground-based remotely sensed measurements of water (vapour, liquid, and solid), temperature, and net surface radiation have been available at Dome C since 2015. Consequently, a comprehensive statistical analysis of the presence of SLW clouds will be performed in the near future. Coupled with modelling studies (NWP ARPEGE-SH, mesoscale models), an estimation of the radiative impact of these clouds on the local climate will then be performed.

Data availability. HAMSTRAD data are available at <http://www.cnrm.meteo.fr/spip.php?article961&lang=en> (Ricaud, 2008). The CALIOP images are accessible at <http://www-calipso.larc.nasa.gov/> (NASA, 2006). The tropospheric depolarization lidar data are reachable at http://lidarmax.altvista.org/englidar/_AntarcticLIDAR.php (Del Guasta, 2008). Radiosondes are available at <http://www.climantartide.it> (Climantartide, 2002). BSRN data can be obtained from the ftp server (<https://bsrn.awi.de/data/data-retrieval-via-ftp/>) (Alfred-Wegener-Institute, 2008). The ARPEGE data and corresponding technical information are available from the YOPP Data Portal and from the ftp server (<ftp://ftp.umr-cnrm.fr/>) (CNRM, 2019) with user “yopp” and password “Arpege”. The NCEP data are available at <https://www.esrl.noaa.gov/psd/> (NOAA, 2020a) and the back trajectory calculations can be performed at <https://www.ready.noaa.gov/HYSPLIT.php> (NOAA, 2020b).

Supplement. The supplement related to this article is available online at: <https://doi.org/10.5194/acp-20-4167-2020-supplement>.

Author contributions. PR, MDG, AL, and PG provided the observational data, while EB, NA, and VG developed the model code and performed the simulations. PD, JLA, and DV contributed to the

data interpretation. All the co-authors participated in the data analysis. PR prepared the paper with contributions from all co-authors. DV, EB, NA, MDG, and PD also contributed significantly to the revision of the paper, supervised by PR.

Competing interests. The authors declare that they have no conflict of interest.

Acknowledgements. The present research project Water Budget over Dome C (H2O-DC) has been approved by the Year of Polar Prediction (YOPP) international committee. The permanently manned Concordia station is jointly operated by the French Institut Paul-Emile Victor (IPEV) and the Italian Programma Nazionale Ricerche in Antartide (PNRA). We would like to thank all the winter personnel who worked at Dome C on the different projects: HAMSTRAD, aerosol lidar, radiosonde, and BSRN. The authors also acknowledge the CALIPSO science team for providing the CALIOP images. We acknowledge the NCEP_Reanalysis 2 data provided by the NOAA/OAR/ESRL PSD, Boulder, Colorado, USA, from their website at <https://www.esrl.noaa.gov/psd/> (last access: 2 April 2020) and the NOAA Air Resources Laboratory for access to the HYSPLIT model through <https://www.ready.noaa.gov/HYSPLIT.php> (last access: 2 April 2020). We would like to thank the two anonymous reviewers for their beneficial comments.

Financial support. This research has been supported by IPEV (French Polar Institute, Institut Paul-Emile Victor) in the framework of the project no. 910 (HAMSTRAD, microwave radiometer) and PNRA (Programma Nazionale di Ricerche in Antartide) in the framework of the projects numbered OSS-006 (BSRN Observatory), AC3.05 (PRE-REC, aerosol lidar), and OSS-10 (RMO OBS, radiosondes).

Review statement. This paper was edited by Corinna Hoose and reviewed by two anonymous referees.

References

- Adhikari, L., Wang, Z., and Deng, M.: Seasonal variations of Antarctic clouds observed by CloudSat and CALIPSO satellites, *J. Geophys. Res.*, 117, D04202, <https://doi.org/10.1029/2011JD016719>, 2012.
- Alfred-Wegener-Institute: Baseline Surface Radiation Network (BSRN), available at: <https://bsrn.awi.de/data/data-retrieval-via-ftp/> (last access: 3 April 2020), 2008.
- Argentini, S., Viola, A., Sempreviva, A. M., and Petenko, I.: Summer boundary-layer height at the plateau site of Dome C, Antarctica, *Bound.-Lay. Meteorol.*, 115, 409–422, 2005.
- Bromwich, D. H., Nicolas, J. P., Hines, K. M., Kay, J. E., Key, E. L., Lazzara, Lubin, D., McFarquhar, G. M., Gorodetskaya, I. V., Grosvenor, D. P., Lachlan-Cope, T., and van Lipzig, N. P. M.: Tropospheric clouds in Antarctica, *Rev. Geophys.*, 50, RG1004, <https://doi.org/10.1029/2011RG000363>, 2012.

- Bromwich, D. H., Otieno, F. O., Hines, K. M., Manning, K. W., and Shilo, E.: Comprehensive evaluation of polar weather research and forecasting model performance in the Antarctic, *J. Geophys. Res.-Atmos.*, 118, 274–292, 2013.
- Casasanta, G., Pietroni, I., Petenko, I., and Argentini, S.: Observed and modelled convective mixing-layer height at Dome C, Antarctica, *Bound.-Lay. Meteorol.*, 151, 597–608, 2014.
- Climantartide: Osservatorio Meteo-Climatologico Antartico, available at: <http://www.climantartide.it/> (last access: 3 April 2020), 2002.
- CNRM: YOPP ARPEGE data, available at: <ftp://ftp.umr-cnrm.fr> (last access: 3 April 2020) with user “yopp” and password “Arpege”, 2019.
- Del Guasta, M.: INO LIDAR in Antarctica, available at: http://lidarmax.altervista.org/englidar/_AntarcticLIDAR.php (last access: 3 April 2020), 2008.
- Driemel, A., Augustine, J., Behrens, K., Colle, S., Cox, C., Cuevas-Agulló, E., Denn, F. M., Duprat, T., Fukuda, M., Grobe, H., Haefelin, M., Hodges, G., Hyett, N., Ijima, O., Kallis, A., Knap, W., Kustov, V., Long, C. N., Longenecker, D., Lupi, A., Maturilli, M., Mimouni, M., Ntsangwane, L., Ogihara, H., Olano, X., Olfes, M., Omori, M., Passamani, L., Pereira, E. B., Schmithüsen, H., Schumacher, S., Sieger, R., Tamlyn, J., Vogt, R., Vuilleumier, L., Xia, X., Ohmura, A., and König-Langlo, G.: Baseline Surface Radiation Network (BSRN): structure and data description (1992–2017), *Earth Syst. Sci. Data*, 10, 1491–1501, <https://doi.org/10.5194/essd-10-1491-2018>, 2018.
- Goy, C., Potenza, M. A., Dederá, S., Tomut, M., Guillerm, E., Kalinin, A., Voss, K.-O., Schottelius, A., Petridis, N., Prosvetov, A., Tejada, G., Fernández, J. M., Trautmann, C., Caupin, F., Glasmacher, U., and Grisenti, R. E.: Shrinking of rapidly evaporating water microdroplets reveals their extreme supercooling, *Phys. Rev. Lett.*, 120, 015501, <https://doi.org/10.1103/PhysRevLett.120.015501>, 2018.
- Grazioli, J., Genthon, C., Boudevillain, B., Duran-Alarcon, C., Del Guasta, M., Madeleine, J.-B., and Berne, A.: Measurements of precipitation in Dumont d’Urville, Adélie Land, East Antarctica, *The Cryosphere*, 11, 1797–1811, <https://doi.org/10.5194/tc-11-1797-2017>, 2017.
- Grosvenor, D. P., Choularton, T. W., Lachlan-Cope, T., Gallagher, M. W., Crosier, J., Bower, K. N., Ladkin, R. S., and Dorsey, J. R.: In-situ aircraft observations of ice concentrations within clouds over the Antarctic Peninsula and Larsen Ice Shelf, *Atmos. Chem. Phys.*, 12, 11275–11294, <https://doi.org/10.5194/acp-12-11275-2012>, 2012.
- Hogan, R. J. and Illingworth, A. J.: The effect of specular reflection on spaceborne lidar measurements of ice clouds, Report of the ESA Retrieval algorithm for EarthCARE project, 5 pp., 2003.
- Kanamitsu, M., Ebisuzaki, W., Woollen, J., Yang, S.-K., Hnilo, J. J., Fiorino, M., and Potter, G. L.: NCEP-DOE AMIP-II Reanalysis (R-2), *B. Am. Meteorol. Soc.*, 83, 1631–1643, <https://doi.org/10.1175/BAMS-83-11-1631>, 2002.
- King, J. C., Argentini, S. A., and Anderson, P. S.: Contrasts between the summertime surface energy balance and boundary layer structure at Dome C and Halley stations, Antarctica, *J. Geophys. Res.-Atmos.*, 111, D02105, <https://doi.org/10.1029/2005JD006130>, 2006.
- King, J. C., Gadian, A., Kirchgassner, A., Kuipers Munneke, P., Lachlan-Cope, T. A., Orr, A., Reijmer, C., Broeke, M. R., van Wessem, J. M., and Weeks, M.: Validation of the summertime surface energy budget of Larsen C Ice Shelf (Antarctica) as represented in three high-resolution atmospheric models, *J. Geophys. Res.-Atmos.*, 120, 1335–1347, <https://doi.org/10.1002/2014JD022604>, 2015.
- Lachlan-Cope, T.: Antarctic clouds, *Polar Res.*, 29, 150–158, 2010.
- Lachlan-Cope, T., Listowski, C., and O’Shea, S.: The microphysics of clouds over the Antarctic Peninsula – Part 1: Observations, *Atmos. Chem. Phys.*, 16, 15605–15617, <https://doi.org/10.5194/acp-16-15605-2016>, 2016.
- Lawson, R. P. and Gettelman, A.: Impact of Antarctic mixed-phase clouds on climate, *P. Natl. Acad. Sci. USA*, 111, 18156–18161, 2014.
- Legrand, M., Yang, X., Preunkert, S., and Therys, N.: Year-round records of sea salt, gaseous, and particulate inorganic bromine in the atmospheric boundary layer at coastal (Dumont d’Urville) and central (Concordia) East Antarctic sites, *J. Geophys. Res.-Atmos.*, 121, 997–1023, <https://doi.org/10.1002/2015JD024066>, 2016.
- Listowski, C. and Lachlan-Cope, T.: The microphysics of clouds over the Antarctic Peninsula – Part 2: modelling aspects within Polar WRF, *Atmos. Chem. Phys.*, 17, 10195–10221, <https://doi.org/10.5194/acp-17-10195-2017>, 2017.
- Listowski, C., Delanoë, J., Kirchgassner, A., Lachlan-Cope, T., and King, J.: Antarctic clouds, supercooled liquid water and mixed phase, investigated with DARDAR: geographical and seasonal variations, *Atmos. Chem. Phys.*, 19, 6771–6808, <https://doi.org/10.5194/acp-19-6771-2019>, 2019.
- Lubin, D., Chen, B., Bromwich, D. H., Somerville, R. C., Lee, W. H., and Hines, K. M.: The Impact of Antarctic Cloud Radiative Properties on a GCM Climate Simulation, *J. Climate*, 11, 447–462, 1998.
- Miloshevich, L. M., Vömel, H., Whiteman, D. N., Lesht, B. M., Schmidlin, F. J., and Russo, F.: Absolute accuracy of water vapor measurements from six operational radiosonde types launched during AWEX-G and implications for AIRS validation, *J. Geophys. Res.*, 111, D09S10, <https://doi.org/10.1029/2005JD006083>, 2006.
- Miloshevich, L. M., Vömel, H., Whiteman, D. N., and Leblanc, T.: Accuracy assessment and corrections of Vaisala RS92 radiosonde water vapour measurements, *J. Geophys. Res.*, 114, D11305, <https://doi.org/10.1029/2008JD011565>, 2009.
- Mishchenko, M. I., Hovenier, J. W., and Travis, L. D. (Eds.): *Light Scattering by Nonspherical Particles: Theory, Measurements, and Applications*, Academic Press, chap. 14, 393–416, 2000.
- NASA: Cloud-Aerosol Lidar and Infrared Pathfinder Satellite Observation (CALIPSO), available at: <https://www-calipso.larc.nasa.gov/> (last access: 3 April 2020), 2006.
- NOAA: ESRL Physical Sciences Division, NCEP data, available at: <https://www.esrl.noaa.gov/psd/>, last access: 3 April 2020a.
- NOAA: Air Resources Laboratory, HYSPLIT model, available at: <https://www.ready.noaa.gov/HYSPLIT.php>, last access: 3 April, 2020b.
- O’Shea, S. J., Choularton, T. W., Flynn, M., Bower, K. N., Gallagher, M., Crosier, J., Williams, P., Crawford, I., Fleming, Z. L., Listowski, C., Kirchgassner, A., Ladkin, R. S., and Lachlan-Cope, T.: In situ measurements of cloud microphysics and aerosol over coastal Antarctica during the

- MAC campaign, *Atmos. Chem. Phys.*, 17, 13049–13070, <https://doi.org/10.5194/acp-17-13049-2017>, 2017.
- Pailleux, J., Geleyn, J.-F., El Khatib, R., Fischer, C., Hamrud, M., Thépaut, J.-N., Rabier, F., Andersson, E., Salmond, D., Burridge, D., Simmons, A., and Courtier, P.: Les 25 ans du système de prévision numérique du temps IFS/Arpège, *La Météorologie*, 89, 18–27, <https://doi.org/10.4267/2042/56594>, 2015.
- Palchetti, L., Bianchini, G., Di Natale, G., and Del Guasta, M.: Far infrared radiative properties of water vapor and clouds in Antarctica, *B. Am. Meteorol. Soc.*, 96, 1505–1518, <https://doi.org/10.1175/BAMS-D-13-00286.1>, 2015.
- Pruppacher, H. R. and Klett, J. D.: *Microphysics of Clouds and Precipitation*: Reprinted 1980, Springer Science & Business Media, Second revised and enlarged edition, 2012.
- Ricaud, P.: HAMSTRAD, H₂O Antarctica Microwave Stratospheric and Tropospheric Radiometers, available at: <http://www.cnrm.meteo.fr/spip.php?article961&lang=en> (last access: 2 April, 2020), 2008.
- Ricaud, P., Gabard, B., Derrien, S., Chaboureaud, J.-P., Rose, T., Mombauer, A., and Czekala, H.: HAMSTRAD-Tropo, A 183-GHz Radiometer Dedicated to Sound Tropospheric Water Vapor Over Concordia Station, Antarctica, *IEEE T. Geosci. Remote*, 48, 1365–1380, <https://doi.org/10.1109/TGRS.2009.2029345>, 2010a.
- Ricaud, P., Gabard, B., Derrien, S., Attié, J.-L., Rose, T., and Czekala, H.: Validation of tropospheric water vapor as measured by the 183-GHz HAMSTRAD Radiometer over the Pyrenees Mountains, France, *IEEE T. Geosci. Remote*, 48, 2189–2203, 2010b.
- Ricaud, P., Genthon, C., Durand, P., Attié, J.-L., Carminati, F., Canut, G., Vanacker, J.-F., Moggio, L., Courcoux, Y., Pellegrini, A., and Rose, T.: Summer to Winter Diurnal Variabilities of Temperature and Water Vapor in the lowermost troposphere as observed by the HAMSTRAD Radiometer over Dome C, Antarctica, *Bound.-Lay. Meteorol.*, 143, 227–259, <https://doi.org/10.1007/s10546-011-9673-6>, 2012.
- Ricaud, P., Carminati, F., Attié, J.-L., Courcoux, Y., Rose, T., Genthon, C., Pellegrini, A., Tremblin, P., and August, T.: Quality Assessment of the First Measurements of Tropospheric Water Vapor and Temperature by the HAMSTRAD Radiometer over Concordia Station, Antarctica, *IEEE T. Geosci. Remote*, 51, 3217–3239, <https://doi.org/10.1109/TGRS.2012.2225627>, 2013.
- Ricaud, P., Grigioni, P., Zbinden, R., Attié, J.-L., Genoni, L., Galeandro, A., Moggio, A., Montaguti, S., Petenko, I., and Legovini, P.: Review of tropospheric temperature, absolute humidity and integrated water vapour from the HAMSTRAD radiometer installed at Dome C, Antarctica, 2009–14, *Antarct. Sci.*, 27, 598–616, <https://doi.org/10.1017/S0954102015000334>, 2015.
- Ricaud, P., Bazile, E., del Guasta, M., Lanconelli, C., Grigioni, P., and Mahjoub, A.: Genesis of diamond dust, ice fog and thick cloud episodes observed and modelled above Dome C, Antarctica, *Atmos. Chem. Phys.*, 17, 5221–5237, <https://doi.org/10.5194/acp-17-5221-2017>, 2017.
- Rolph, G., Stein, A., and Stunder, B.: Real-time Environmental Applications and Display sYstem: READY, *Environ. Modell. Softw.*, 95, 210–228, <https://doi.org/10.1016/j.envsoft.2017.06.025>, 2017.
- Stein, A. F., Draxler, R. R., Rolph, G. D., Stunder, B. J. B., Cohen, M. D., and Ngan, F.: NOAA's HYSPLIT atmospheric transport and dispersion modeling system, *B. Am. Meteorol. Soc.*, 96, 2059–2077, <https://doi.org/10.1175/BAMS-D-14-00110.1>, 2015.
- Stull, R. B.: *An introduction to boundary layer meteorology*, Vol. 13, Springer Science & Business Media, 2012.
- Tomasi, C., Petkov, B., Mazzola, M., Ritter, C., di Sarra, A., di Iorio, T., and del Guasta, M.: Seasonal variations of the relative optical air mass function for background aerosol and thin cirrus clouds at Arctic and Antarctic sites, *Remote Sensing*, 7, 7157–7180, 2015.
- Winker, D. M., Vaughan, M. A., Omar, A., Hu, Y., Powell, K. A., Liu, Z., Hunt, W. H., and Young, S. A.: Overview of the CALIPSO mission and CALIOP data processing algorithms, *J. Atmos. Ocean. Tech.*, 26, 2310–2323, 2009.
- Young, G., Jones, H. M., Choullarton, T. W., Crosier, J., Bower, K. N., Gallagher, M. W., Davies, R. S., Renfrew, I. A., Elvidge, A. D., Darbyshire, E., Marengo, F., Brown, P. R. A., Ricketts, H. M. A., Connolly, P. J., Lloyd, G., Williams, P. L., Allan, J. D., Taylor, J. W., Liu, D., and Flynn, M. J.: Observed microphysical changes in Arctic mixed-phase clouds when transitioning from sea ice to open ocean, *Atmos. Chem. Phys.*, 16, 13945–13967, <https://doi.org/10.5194/acp-16-13945-2016>, 2016.
- Young, G., Lachlan-Cope, T., O'Shea, S. J., Dearden, C., Listowski, C., Bower, K. N., Choullarton, T. W., and Gallagher, M. W.: Radiative effects of secondary ice enhancement in coastal Antarctic clouds, *Geophys. Res. Lett.*, 46, 2312–2321, <https://doi.org/10.1029/2018GL080551>, 2019.
- Young, S. A. and Vaughan, M. A.: The retrieval of profiles of particulate extinction from Cloud Aerosol Lidar Infrared Pathfinder Satellite Observations (CALIPSO) lidar data: Algorithm description, *J. Atmos. Ocean. Tech.*, 26, 1105–1119, 2009.